INVESTIGATING THE EFFECT OF LACUNOCANALICULAR NETWORK MORPHOLOGY ALTERATION DUE TO AGING ON OSTEOCYTE FFSS USING COMPUTATIONAL MODELING

A DISSERTATION IN

Engineering

&

Oral and Craniofacial Sciences

Presented to the Faculty of the University
of Missouri-Kansas City in partial fulfillment of
the requirements for the degree

DOCTOR OF PHILOSOPHY

By

MOHAMMADMEHDI NIROOBAKHSH

B.Sc., Semnan University, Tehran, IRAN, 2013

M.Sc., Iran University of Science & Technology, Tehran, IRAN, 2016

Kansas City, Missouri

2022

INVESTIGATING THE EFFECT OF LACUNOCANALICULAR NETWORK MORPHOLOGY ALTERATION DUE TO AGING ON OSTEOCYTE FFSS USING COMPUTATIONAL MODELING

Mohammadmehdi Niroobakhsh, Candidate for the Doctor of Philosophy Degree

University of Missouri-Kansas City, 2022

ABSTRACT

Exercise and physical activity exert mechanical loading on the bones, stimulating bone formation. Osteocytes are thought to be the bone cells that sense and respond to mechanical loading and that loading induces bone strains and fluid flow shear stresses (FFSS) on the osteocytes. However, how the complex morphology of the osteocyte lacunocanalicular network affects local stresses and strains experienced by the osteocytes is not fully understood.

In this study, we assessed the effect of morphological parameters including canalicular density, lacunocanalicular space thickness, dendrite diameter, number of fluid inlets to the lacuna, and load direction on FFSS and bone strains and how these might change with the microstructural deterioration of the LCN that occurs with aging. Four distinct theoretical models were initially created of osteocytes with either ten or eighteen dendrites using a fluid-structure interaction (FSI) method with idealized geometries. Next, two models of young and aged osteocytes were developed from 3D confocal images after FITC staining of the LCN in the femur of a 5-month-old and 22-month-old C57BL6 mouse. Also, several simulated osteocyte models were developed from confocal images of a 4-month-old C57BL6 mouse using a geometry modification approach to model different LCN morphologies. Shear stresses on osteocyte and dendritic membranes were estimated using a computational fluid dynamics (CFD) approach considering the average surface area and volume of each model.

The models predicted higher fluid velocity in the canaliculi versus the lacuna. Comparison of idealized models with one fluid inlet versus five fluid inlets indicated that the average shear stress increased from 0.13 Pa to 0.28 Pa and one-half of the dendrites experienced FFSS greater than 0.8 Pa with four more fluid inlets. The 3D simulations of models based on confocal images of osteocytes indicated that the velocity profile alters in the tortuous canaliculi, near canalicular branches, and canalicular junctions. Our findings indicate not only a higher ratio of canalicular to lacunar surface area in the young osteocyte model than in the aged model but also a greater average FFSS in the young model than the aged model. Consequently, osteocytes experience lower shear stresses on the osteocyte body and dendritic membranes in the aged models. Importantly, the surface area of the young osteocyte model with required shear stress for osteocyte response was 23 times greater than the aged osteocyte. Therefore, aged osteocyte is less possible to detect mechanical strains due to lower dendritic surface area which explains the lower mechanoresponsiveness of osteocytes with aging with the same physiological activity. We also predicted that with increasing canalicular density or lacunocanalicular space thickness, FFSS experienced by osteocytes increases. Both the realistic aged osteocyte model generated from confocal images of an aged mouse and the simulated aged osteocyte model generated from confocal images of a young mouse using the geometry modification technique showed similar FFSS results. This study shows the significance of this technique in computer modeling of osteocytes. Overall, this modeling approach based on accurate osteocyte morphologies, may explain the impaired mechano-responsiveness of the osteocytes with aging and could be a powerful tool to predict the effect of bone diseases on osteocyte mechanoresponsive ness.

APPROVAL PAGE

The faculty listed below, appointed by the Dean of the School of Graduate Studies have examined a thesis titled 'Investigating the Effect of LCN Morphology Alteration Due to Aging or Bone Disease on Osteocyte FFSS Using Computational Modeling' presented by Mohammad Niroobakhsh, candidate for the Doctor of Philosophy degree, and certify that in their opinion it is worthy of acceptance.

Supervisory Committee

Thiagarajan Ganesh, Ph. D., P.E., Committee Chair
Department of Civil Engineering

Mark L. Johnson, Ph.D.,
Department of Oral Biology and Craniofacial Sciences

Sarah L. Dallas, Ph.D.,
Department of Oral Biology and Craniofacial Sciences

Gregory King, Ph.D.,
Department of Mechanical Engineering

Antonis Stylianou, Ph.D.,
Department of Mechanical Engineering

TABLE OF CONTENTS

LIST OF ILLUSTRATIONS

Figure Page

LIST OF TABLES

Table Page

ACKNOWLEDGEMENTS

First, thank God for blessing me with the completion of this research at UMKC. I wish to express my sincere gratitude to my supervisor, Dr. Ganesh Thiagarajan, for his advice, support, and encouragement. His knowledge and incentive inspired me in many ways and helped me through the difficulties I encountered during my PhD program.

I am also grateful to Dr. Mark L. Johnson, Dr. Sarah Dallas, Dr. Gregory King, and Dr. Antonis Stylianou, for serving on my supervisory committee and for their valuable inputs on my research.

Finally, my deep and sincere gratitude to my family for their continuous and unparalleled love, help and support. I want to say thanks to my parents, especially my mother who passed away in the middle of my Ph.D. for encouraging me to see dreams and follow them. I am grateful to my sisters for always being there for me as a friend. I am forever indebted to my family for giving me the opportunities and experiences that have made me who I am.

1 CHAPTER1: INTRODUCTION

Reduced bone mass is a common feature of advancing age that can result in osteoporosis and increased bone fragility. Osteoporotic fractures, which occur in a variety of bones such as spine, hip, and wrist usually lead to loss of mobility and can reduce the patient's quality of life [1]. Noh et al. reported that 200 million people worldwide suffer from osteoporosis and that one in every three women over age 50 and one in every five men over 50 worldwide experience osteoporosis-related bone fractures in their lives [2]. Several variables including lack of calcium, estrogen deficiency, low vitamin D levels, and reduced physical activity contribute to aging-associated bone loss which results in changes in bone architecture and mechanical properties [3-5].

Osteocytes are the most abundant cells in bone and are thought to be the mechanoresponsive cells that sense mechanical loading due to physical activity and initiate biochemical signaling through a process called mechanotransduction that results in bone formation (reviewed in [6]). Osteocytes are connected by an intricate network of dendritic processes. The dendrites reside inside channels in the bone, called canaliculi, and the fluid flows around the dendrites and through the canaliculi. It has been postulated that osteocytes detect mechanical loads due to fluid flow shear stress (FFSS) generated in the lacunocanalicular network (LCN) around the osteocyte dendritic processes and to local strains around the osteocyte cell body [7-9]. Mechanical loading of bone generates a pressure gradient that initiates interstitial fluid flow in the LCN and across the osteocyte cell membrane and dendritic surfaces. Several models have hypothesized that FFSS on the osteocytes and their dendrites causes cell membrane deformation and initiates biochemical signaling [7, 10, 11].

Whole bone is postulated to undergo fracture damage *in vivo* at surface strains with a magnitude of 3,500 microstrain or greater, while paradoxically, *in vitro* studies with bone cells have shown that 5,000 microstrain is required to cause some cellular response and strains over 10,000 microstrain cause a significant osteogenic response [12-14]. Similarly, analytical models predicted that the required fluid-induced shear stress to increase bone mass is 0.8 Pa [9, 15]. Nicolella et al. used a digital image correlation measurement technique to show that local strains around the lacuna could reach 30,000 microstrain which is over an order of magnitude greater than the global strain of 1,500 - 2,000 microstrain needed to induce bone formation [16].

Bone microstructure undergoes degenerative changes in osteocyte and LCN morphology with aging [17-20] (reviewed in [21]). This deterioration in osteocyte dendrite connectivity may contribute to age-related bone loss, potentially due to impaired mechano-responsiveness through disruption of osteocyte regulation of osteoblast and osteoclast function—however, the osteocyte network's inaccessibility in the bone matrix limits *in vivo* experiments. Finding a link between load-induced fluid flow on the osteocytes and their mechano-sensitivity regarding LCN morphology could bridge the knowledge gap between mechanical load and bone formation.

To overcome some of the limitations of *in vivo* studies of FFSS within the LCN we have used a computer modeling approach combining fluid-structure interaction (FSI) and computational fluid dynamics (CFD) analysis. In terms of the intricacy of bone architecture, most numerical models reconstruct either fluid or solid domains of the osteocyte and its surroundings. Anderson et al. developed a CFD model of an osteocyte at the micro/nano-scale and predicted the highest FFSS occurs on the dendrites rather than osteocyte [22]. Multiphysics

FSI modeling is considered a valuable tool to mimic the mechanical behavior of the osteocyte. An idealized osteocyte FSI model was developed for the first time by Verbruggen et al., and the mechanical stimulation of the osteocytes was investigated [23]. Simulations under mechanical loading predicted that maximum stimulus occurs on the cell processes. More realistic osteocyte models predict higher strains, shear stresses, and fluid velocities than those from idealized models [24, 25].

The LCN complexity can be defined based on the number and extent of branching per canaliculi [26]. A single osteocyte dendrite may develop numerous branches, creating a matrix of intercommunication between osteocytes. The number of secondary canaliculi is about four times greater than that of primary canaliculi per lacuna [27]. Schurman et al., using a structural analysis, showed that the LCN in cortical bone experiences pruning due to aging together with dendritic system degradation [18].

The significance of load direction on osteocytes was studied by Kola et al., who built 2D finite element models of idealized osteocytes to analyze strains based on lacunar orientation. They predicted that the lacunar strains are higher when lacunae are aligned perpendicular to the loading axis [28]. Rath Bonivtch et al. developed a 3D model of the osteocyte and showed that either increasing the canalicular diameter or decreasing the perilacunar tissue modulus increases the maximum strain experienced by the perilacunar region [29].

Bonewald et al. have suggested that depending on the cell and LCN topology, different bone cells receive different magnitudes of fluid shear stress [30]. Joukar et al. investigated the influence of osteocyte morphology and loading direction on cell stimulation by including ECM projections using an idealized 3D FSI model. They showed that FFSS on the dendrites along the loading direction, and osteocytes with a major axis aligned to the loading direction is higher than in other cases [31]. Kamioka et al. demonstrated the critical influence of osteocyte shape on cell process fluid velocities [32]. However, how the number of canaliculi is correlated to shear stress and bone strains at a microscopic scale has not been established.

Due to the complexity of bone structure, researchers employ various simplification techniques in computer simulations to achieve an idealized morphology. Utilizing actual biological data is a step toward clarifying the role of osteocytes in the bone physiological response to loading. More realistic image-derived models that include LCN shape and canalicular tortuosity [18, 23, 33] can assess the cell's response to mechanical stress better than idealized geometries. However, replicating the osteocyte microenvironment precisely requires high-resolution images of the lacunocanalicular system. Various standard imaging techniques are employed to visualize osteocytes in bone, such as confocal laser scanning microscopy (CLSM), scanning electron microscopy (SEM), and transmission electron microscopy (TEM) [34]. Tiny cell processes can be captured using advanced imaging techniques and used in image-derived simulations [24, 35].

The objective of this research is to investigate the effect of LCN deterioration due to aging or other bone disease in terms of reduction in canalicular density or surface area and the resulting changes in shear stresses that would be experienced by osteocyte and their dendrites. Multiple theoretical FSI models using idealized geometries were generated to investigate the FFSS and bone strains in terms of the significance of physiological parameters, including canalicular density, load direction, and the number of fluid flow inlets to the lacuna, which had never been explored previously. Then, confocal image derived CFD models associated with a single osteocyte representing a young and an aged osteocyte and some simulated osteocyte models were built to compare shear forces while accounting for increased canalicular density, dendrite diameter, and lacunocanalicular space thickness due to aging, which is not conducive to direct measurement. These simulations reveal the amount of the entire osteocyte model that experiences FFSS magnitudes needed to trigger biochemical signaling and how aging or bone disease alters this strain threshold. Furthermore, the models identify the significance of volume and surface area of the lacunocanalicular space around the osteocyte and dendrites on FFSS.

The materials and methods used for developing the osteocyte models are described in Chapter two. This part deals with the methods used to prepare bone samples and obtain confocal images of osteocytes. The stepwise procedure to prepare bone samples for confocal microscopy includes fixing the bone, embedding in acrylic, sectioning, and polishing, staining with FITC dye, and finally, confocal microscopy. The methods to develop three-dimensional models of osteocytes utilizing various biology and engineering softwares are also described in this chapter. Various osteocyte models with either idealized, confocal image-based, and simulated geometries using geometry modification techniques are presented. At the end, the method to generate mesh, boundary conditions, and setup for FSI and Computational Fluid Dynamics (CFD) analysis using ANSYS software is described.

Chapter three details the results obtained from the computer simulations described in chapter two. The velocity, shear stress, and mechanical strain contours produced by the osteocyte and inside the lacunocanalicular space are illustrated for each model considering their lacunocanalicular network volume and surface area. The idealized and realistic osteocyte models are treated separately considering their geometrical differences. Furthermore, osteocyte models generated using different approaches are compared.

The fourth chapter covers all the discussion of the results presented in the third chapter. The primary goal of this chapter is providing explanations on the results in chapter three and to have a better understanding of how the morphological changes in the lacunocanalicular system due to aging or bone disease could be related to the shear stress and strains produced by the osteocytes. Additionally, the correlation of these morphological changes with stress is discussed and the most significant geometrical parameters affecting the shear stress are determined.

The fifth chapter summarizes the findings of this dissertation as well as the scope of future work. The details of how this work can be valuable in understanding aging or other bone disease such as osteoporosis are also given in this chapter. Future studies using accurate 3D models based on empirical data rather than idealized geometries can help understand the effects of bone diseases on bone mechanoresponsiveness and osteocyte function.

2 CHAPTER 2: METHODS

This Chapter outlines the design of the entire study. The method to develop 3D models of osteocytes using idealized, confocal image-based geometries, and simulated models using geometry modification technique is explained and various approaches such as fluid-structure interaction and computational fluid dynamics to measure fluid flow shear stress and bone strains are described. Sample preparation procedure of mouse bones which is a necessary step to visualize osteocytes and obtain confocal images for realistic osteocyte modeling is also explained. Then, the details of software setup to generate mesh and set boundary conditions using ANSYS is elaborated.

2.1 Idealized Osteocyte Models

2.1.1 Geometry Generation

Four computer models of a single osteocyte, each with ten or eighteen dendrites, were constructed in ANSYS SpaceClaim with an idealized osteocyte geometry containing an osteocyte cell body within a lacuna surrounded by interstitial fluid and a bone matrix. (Figure 1). The osteocyte geometry was generated with dimensions similar to the one used by Verbruggen [23]. The major and minor axes of the cells were 13.5 µm and 7.5 µm, while the major and minor axes of the lacuna were 15 µm and 9 µm. The side length of the bone matrix was 21 µm. The osteocyte dendrites and the canaliculi they reside in were set to diameters of 0.44 µm and 0.6 µm, respectively [23]. Magnification of the lacunocanalicular space in Figure 1 indicates that the annular space around the cell is substantially larger than around the cell processes [36, 37].

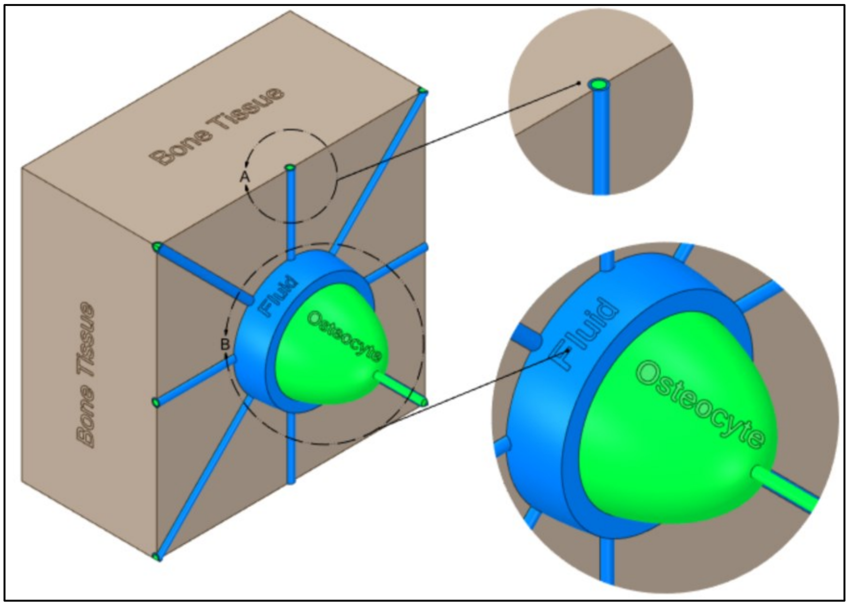

Figure 1: Idealized osteocyte model components, depicting bone tissue (brown), lacunocanalicular space (blue), and osteocyte cell body and dendrites (green). The magnified sections indicate a larger annular space around the cell than the dendrites.

2.1.2 Material Properties and Mesh

Simulated solid material domains, including the osteocyte with its dendrites and bone tissue, were modeled as linearly elastic, isotropic materials. The elastic modulus assigned to the cell was 4.47 kPa with a Poisson's ratio of 0.3. The elastic modulus of the bone tissue was set at 16 GPa with a Poisson's ratio of 0.38 [23]. The LCN fluid is comparable to saltwater, with a density of 997 $\mathrm{kg/m^3}$ and dynamic viscosity of 0.000855 $\mathrm{kg/m^3 s^1}$ [24]. All domains were meshed using tetrahedral elements in the ANSYS software for the Finite Element Analysis. The total number of elements in CFX for the fluid domain is 331,133 and 741,441 for the ten dendrites and eighteen dendrites' models, respectively. Mesh dependency analysis was conducted to ensure that the results do not change with changing the number of mesh elements. With smaller element size that results in greater number of elements (ex, 2,000,000 elements), strain and stress results did not change.

The total elements for solid structures, including cell and bone tissue, are 739,092 and 2,642,352 for the ten and eighteen dendrite models, respectively. Figure 2 and Figure 3 shows the mesh for solid and fluid domains of 10-dendrites and 18-dendrites models, respectively, which was generated in Structural and CFX module of ANSYS workbench software.

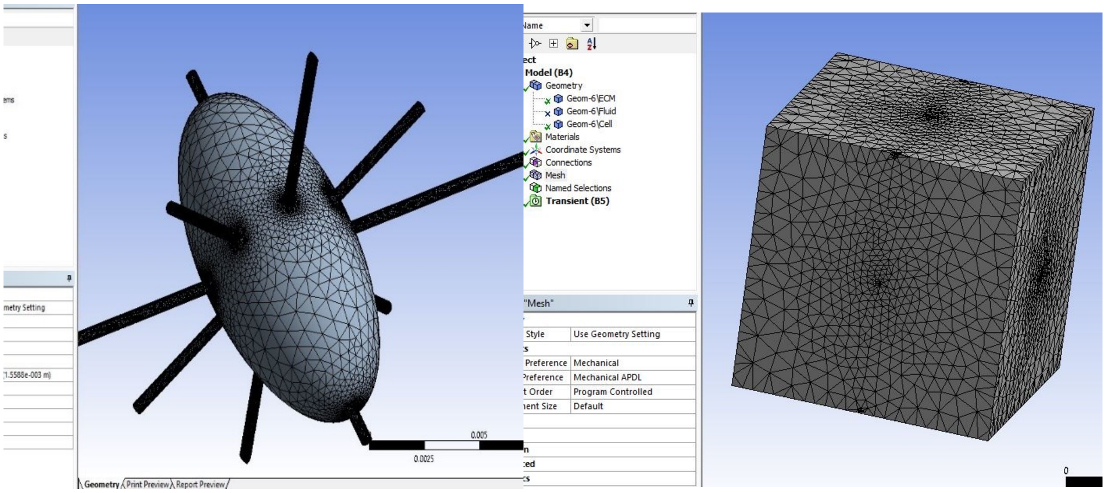

Style	Use Geometry Setting
Preference	Mechanical
Preference	Mechanical APDL
t Order	Program Controlled
nent Size	Default

Figure 2: Mesh generated in ANSYS software for fluid and solid domains of the ten dendrites model.

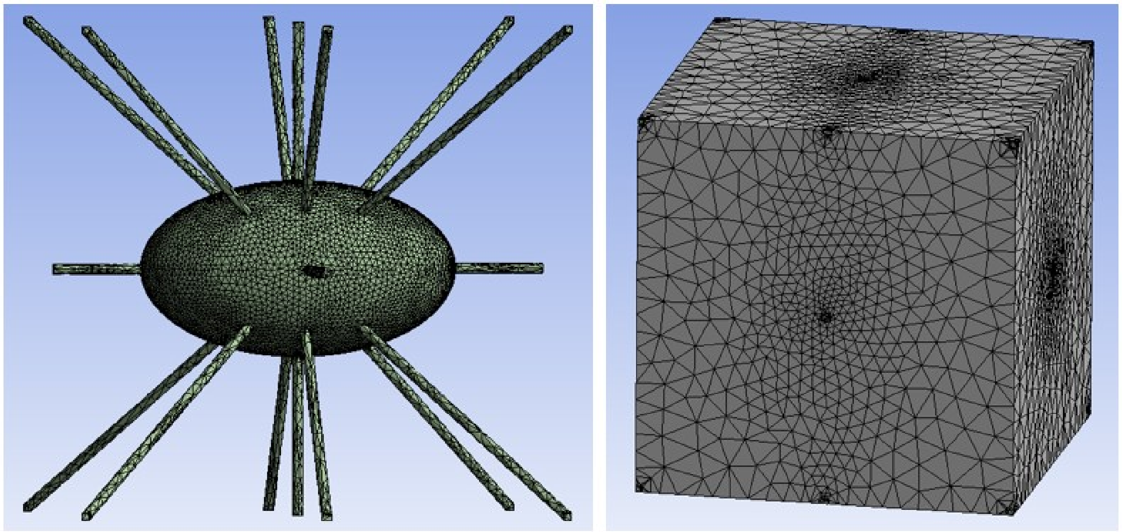

Figure 3: Generated mesh for the fluid and solid domains of eighteen dendrites model.

In the models which include a fluid and a solid interacting with each other, it is critical to use a finer mesh at the interfaces. So, the two domains have a high enough number of elements to interact and transfer the information. Figure 4 indicates the finer mesh at the interface of osteocyte dendrites, fluid domain in the lacunocanalicular space and the bone tissue.

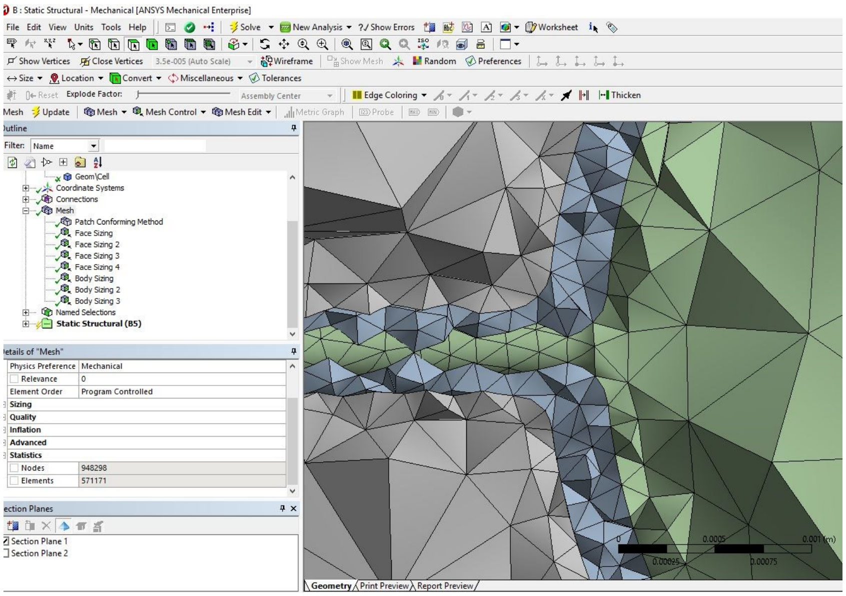

Details of "Mesh"

Physics Preference	Mechanical
☐ Relevance	0
Element Order	Program Controlled
Sizing	
Quality	
Inflation	
Advanced	
Statistics	
☐ Nodes	948298
☐ Elements	571171

Figure 4: A fine mesh was defined at the interfaces of solid and fluid domains

2.1.3 Loading Conditions

The loading conditions used a compressive strain of 3,000 με [38] applied to one side of the solid domains as displacement to mimic vigorous physiological activity, while the opposite side remained fixed. A fluid pressure gradient was exerted across the models to represent load-induced fluid flow. Fluid boundary conditions were specified as 300 Pa of inlet pressure, which is equivalent to the pressure predicted during high-intensity exercise, and outlet pressure was considered 0 Pa [23]. Figure 5 shows the loading conditions which includes a mechanical load (yellow arrow) and a fluid pressure (red circle) at the left face of the model. The right face was fixed and the remaining canaliculi were considered outlets.

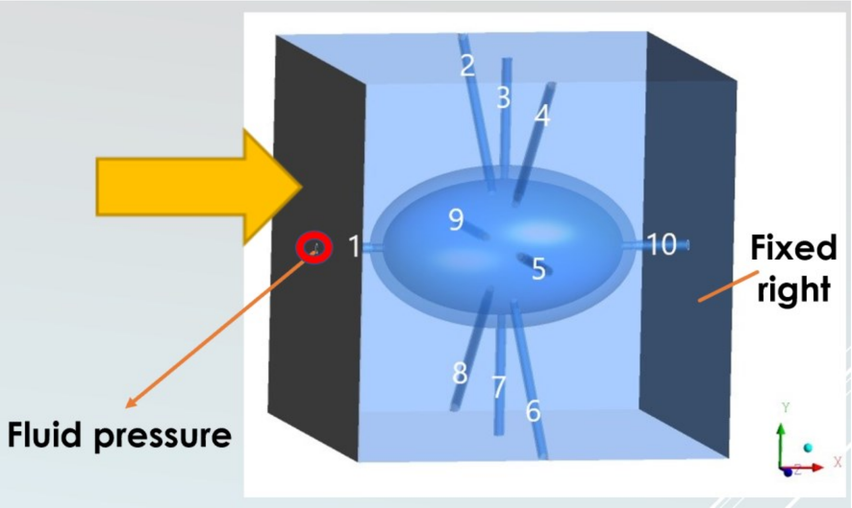

Figure 5: Boundary conditions including a mechanical load and fluid pressure defined for the 10 dendrites osteocyte model where the right side was fixed.

To study each of the three parameters, namely the canalicular density, number of fluid inlets, and load direction, the other two parameters were kept identical, and some boundary conditions changed (Figure 6). For example, Model 1 and Model 2 have the same dendrite number (18 dendrites) and load direction. To compare the effect of the number of inlets on FFSS, Model 1 has five fluid inlets while Model 2 has one fluid inlet. Model 3 was generated with ten dendrites with the same load direction and number of fluid inlets to Model 2. With comparison of Model 2 and Model 3, we analyzed the effect of canalicular density on strain/stress experienced by the osteocyte. We generated Model 4 to determine the outcome of changing the load direction by considering the movement of fluid from the left side of Models 3 and from the top in Model 4. Model 3 and Model 4, each of which has ten dendrites and an equal number of inlets, were compared to examine the effect of load direction.

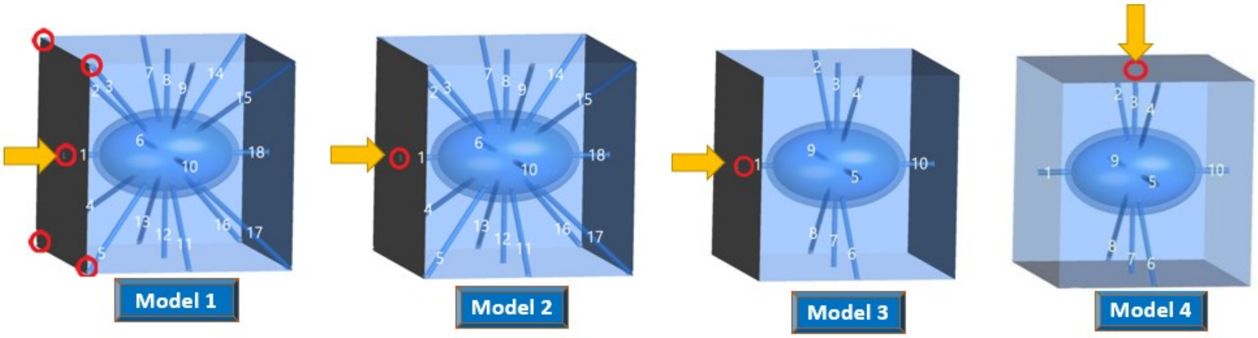

Figure 6: Four osteocyte models with ten or eighteen dendrites, and the load was imposed from either the left side of the solid domains (Models 1-3) or the top side (Model 4), as indicated by an orange arrow. All or one of the canaliculi (circled in red) on the loading face were deemed fluid inlets. The rest of the canaliculi are considered outlets.

2.1.4 Physics Setup

The interfaces of fluid and solid domains are defined and introduced in ANSYS software to interact and transfer the load in each time step. Four different interfaces were defined owing to three domains of cell (osteocyte), fluid, and bone tissue. Solid interfaces were defined in the Structural module and fluid domain was defined in the CFX module of ANSYS. Figure 7 shows how the interfaces were chosen in each geometry of the three different domains. For instance, the inner layer of the fluid domain which is interacting with the cell was selected as the fluid-cell interface and the outer layer of the fluid domain which is interacting with bone tissue was named the fluid-bone interface. The inner layer of the bone domain which was in the interface with the fluid domain was selected as bone-fluid and the outer layer of the cell domain which was interacting with the fluid domain was chosen as cell-fluid.

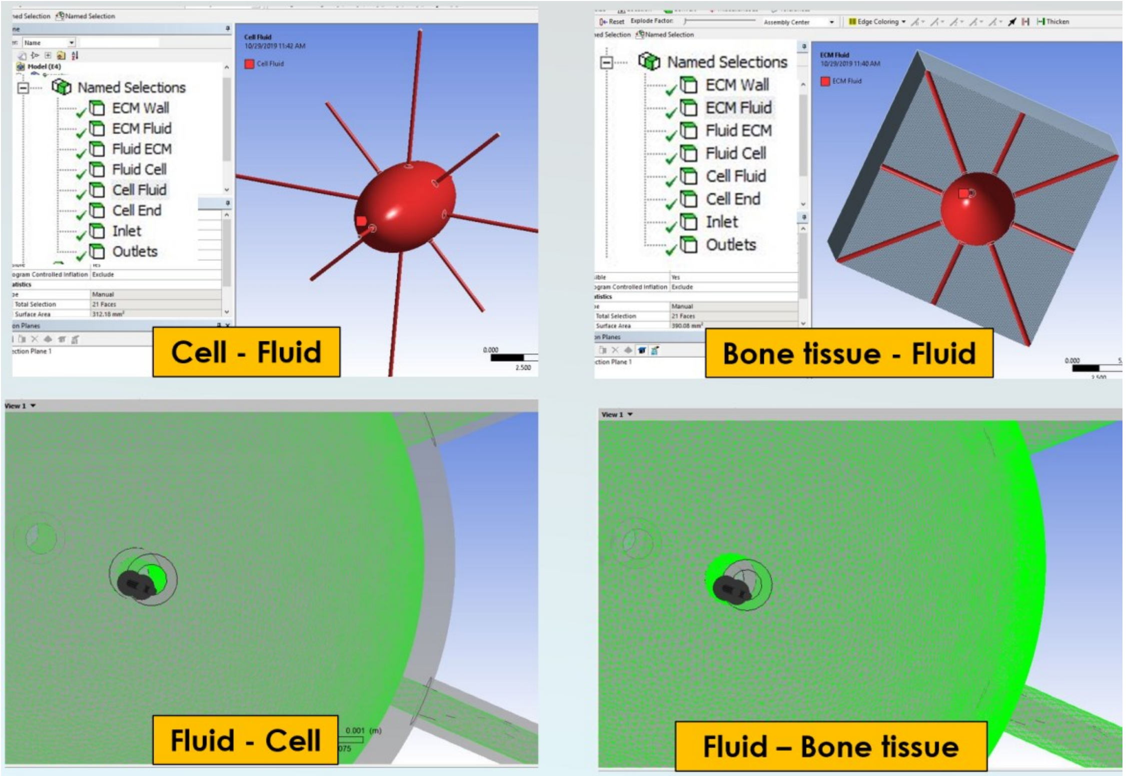

Figure 7: Definition of interfaces of various domains. Four interfaces were defined for three domains of cell, fluid, and bone

2.1.5 Fluid-Structure Interaction (FSI) Analysis

A fluid-structure interaction approach was employed for the Multiphysics morphology of a cell with dendrites, fluid flow within the lacunocanalicular space, and the bone matrix. We employed an FSI approach to provide information about the strain distribution throughout the bone matrix and fluid compartments within the LCN. Two-way FSI was chosen for the coupling for its more realistic solution versus a one-way FSI since it considers the interaction of both domains with the other one. In the two-way FSI method, the interaction of solid and fluid domains is analyzed in the Structural and CFX modules in ANSYS software. By coupling these two modules, Structural module which defines bone and cell domains receives pressure from CFX domain which defines fluid domain and subsequently delivers displacement to CFX as an output. These forces and boundary deformations are transferred between cell, fluid, and bone tissue via four designated interfaces. Therefore, the ANSYS software consistently updates information in the fluid and solid domains at each time step (iteration) until the solution is converged.

2.1.6 System Coupling and Data Transfer

In the FSI problem, besides two different modules of CFX and Structural, a System Coupling module is required to connect and update the information between CFX and Structural modules, which enables solving them simultaneously as one problem. Figure 8 shows that the project schematic consists of two modules of CFX and Structural that were connected using the System Coupling module. The geometries in CFX and Structural were linked and the setup of each of the Transient and CFX was connected directly to the setup of System Coupling module.

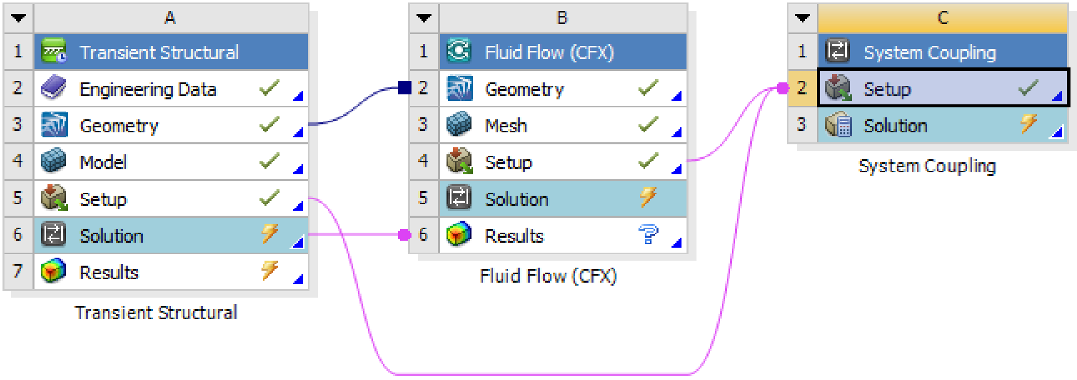

Figure 8: Project schematic for the FSI problem includes three modules of Structural, CFX, and System Coupling

In the system coupling, four interfaces of “cell-fluid”, “fluid-cell”, “fluid-bone”, and “bone-fluid”, which were defined in each of the Structural and CFX modules, were displayed after connecting the setup of two modules to the setup of System Coupling. Since there are four interfaces of fluid and solid domains, four data transfers were defined as shown in Figure 9. Two were for the interfaces of fluid and cell domains and the other two were for the interfaces of fluid and bone domains.

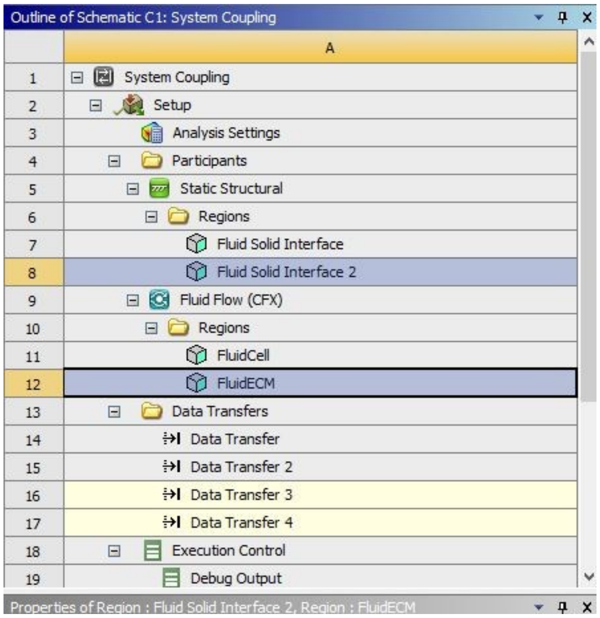

Outline of Schematic C1: System Coupling

	A
1	System Coupling
2	Setup
3	Analysis Settings
4	Participants
5	Static Structural
6	Regions
7	Fluid Solid Interface
8	Fluid Solid Interface 2
9	Fluid Flow (CFX)
10	Regions
11	FluidCell
12	FluidECM
13	Data Transfers
14	Data Transfer
15	Data Transfer 2
16	Data Transfer 3
17	Data Transfer 4
18	Execution Control
19	Debug Output

Properties of Region : Fluid Solid Interface 2, Region : FluidECM

Figure 9: Four Data Transfers created in System Coupling module to connect the information between different domains

Figure 10 shows the properties of Data Transfer1 and Data Transfer 2. Data transfer 1 with Structural as participant, transferred displacements of mesh elements to its target, which was Fluid Flow (CFX). On the other hand, Data Transfer 2 with Fluid Flow (CFX) as participant, transferred Force to its target, which was Structural.

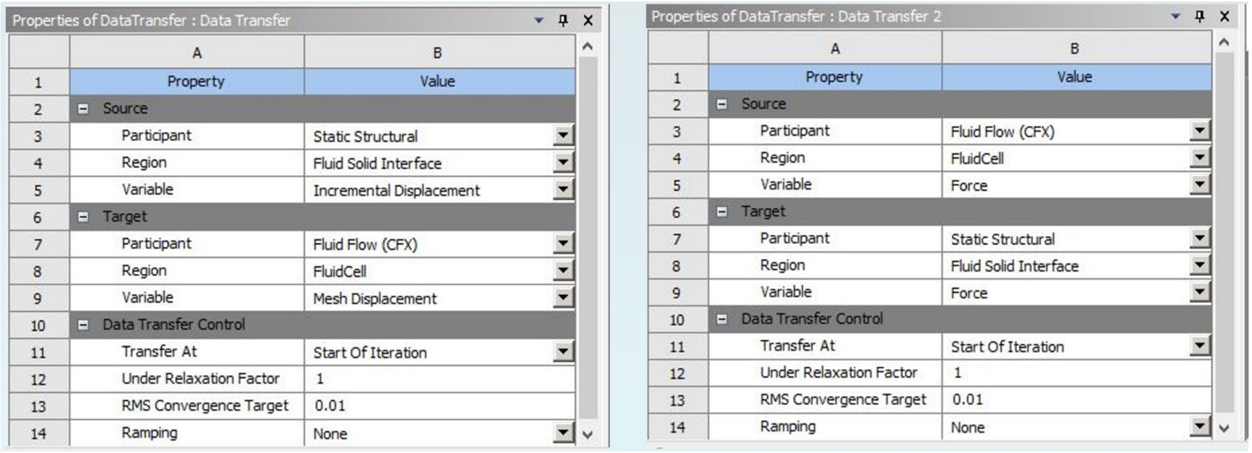

Properties of DataTransfer : Data Transfer

	A	B
1	Property	Value
2	⊟ Source	
3	Participant	Static Structural
4	Region	Fluid Solid Interface
5	Variable	Incremental Displacement
6	⊟ Target	
7	Participant	Fluid Flow (CFX)
8	Region	FluidCell
9	Variable	Mesh Displacement
10	⊟ Data Transfer Control	
11	Transfer At	Start Of Iteration
12	Under Relaxation Factor	1
13	RMS Convergence Target	0.01
14	Ramping	None

Properties of DataTransfer : Data Transfer 2

	A	B
1	Property	Value
2	⊟ Source	
3	Participant	Fluid Flow (CFX)
4	Region	FluidCell
5	Variable	Force
6	⊟ Target	
7	Participant	Static Structural
8	Region	Fluid Solid Interface
9	Variable	Force
10	⊟ Data Transfer Control	
11	Transfer At	Start Of Iteration
12	Under Relaxation Factor	1
13	RMS Convergence Target	0.01
14	Ramping	None

Figure 10: Data transfer properties includes force and displacement information between source and target

After running the software, force and displacement for each of the elements at the interface of solid and fluid domains were updated automatically in each time step until the solutions for each of the modules were converged. Figure 11 shows the System Coupling Solution Information. Once the run is over, the Participant Solution Status presented the convergence for both the Structural and CFX modules.

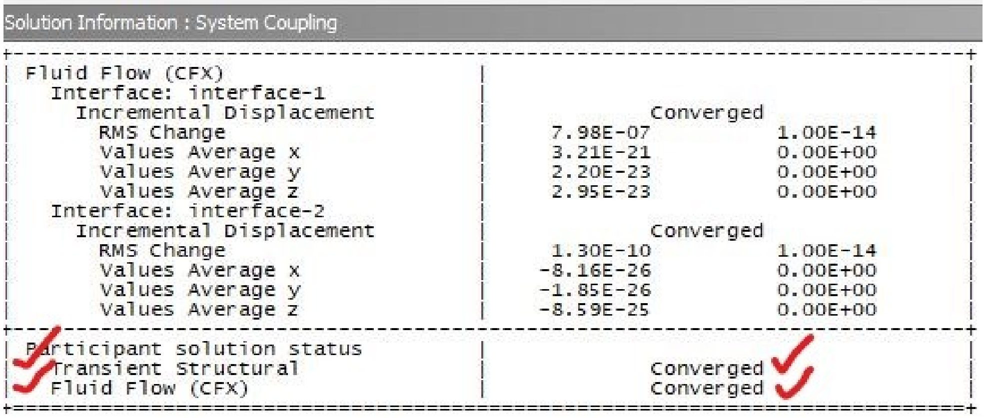

Solution Information : System Coupling

```
+-----------------------------------------------------------------------------+
| Fluid Flow (CFX)                    |                                       |
|   Interface: interface-1            |                                       |
|     Incremental Displacement        |            Converged                  |
|       RMS Change                    |      7.98E-07          1.00E-14       |
|       Values Average x              |      3.21E-21          0.00E+00       |
|       Values Average y              |      2.20E-23          0.00E+00       |
|       Values Average z              |      2.95E-23          0.00E+00       |
|   Interface: interface-2            |                                       |
|     Incremental Displacement        |            Converged                  |
|       RMS Change                    |      1.30E-10          1.00E-14       |
|       Values Average x              |     -8.16E-26          0.00E+00       |
|       Values Average y              |     -1.85E-26          0.00E+00       |
|       Values Average z              |     -8.59E-25          0.00E+00       |
+-----------------------------------------------------------------------------+
| Participant solution status         |                                       |
|   Transient Structural              |            Converged                  |
|   Fluid Flow (CFX)                  |            Converged                  |
+=============================================================================+
```

Figure 11: Solution Information in the System Coupling module showed convergence of both modules

2.2 Confocal Image-Based Osteocyte Models

Bone samples from young and aged mice were fixed, sectioned, and stained for confocal imaging with optical sectioning to generate 3D image stacks. These images were used to build

3D computer models of the lacunocanalicular network. The protocol for imaging and computer modeling will be elaborated in this section.

2.2.1 Sample Preparation

C57Bl/6 mice were obtained from the NIH Mouse Aging Colony at Charles Rivers Laboratories. There were three female mice, one 4-month-old mouse, one 5-month-old mouse, and one 22-month-old mouse. The femur of these mice was chosen for our study and was prepared for confocal microscopy.

First, soft tissue and muscles were removed from the dissected femurs to attain a clean bone. Then, the samples were fixed in 4% PFA at 4 ℃ with gentle shaking for one day and then transferred to 70% EtOH for an additional one day.

The third step was embedding the samples in Acrylic resin. The bones were taken out of 70% EtOH and were embedded in quick embedding medium Sample-Kwick Fast Cure Acrylic Kit (Buehler, Cat No.20-3560), according to manufacturer’s instruction. Two parts of liquid were mixed with two parts of liquid to attain a low viscosity mixture with a higher transparency as the bone sections should be visible to find the third trochanter for the cutting step. It was stirred well for fifteen seconds and poured into a mold that contains bone femurs. The proximal metaphysis was the bottom side and femurs were put vertically into a mold to be sectioned properly in the next step. After the mixture was rapidly polymerized at room temperature for five minutes, the mold was removed. The rapid polymerization resin embedding method is used so that the resin provides adequate support around the bone specimen to facilitate sectioning but does not permeate into the tissue. This is necessary for the subsequent FITC staining step so that the dye can penetrate the lacunae and canaliculi. The fourth step was measuring the bone length and finding the third trochanter of the femurs in the diaphysis region as the trimming line so that sections could be taken from a standardized region of the femur. Three 300µm thick sections were cut toward distal metaphysis using a Leica SP1600 microtome with a cross-section area shown in Figure 12.

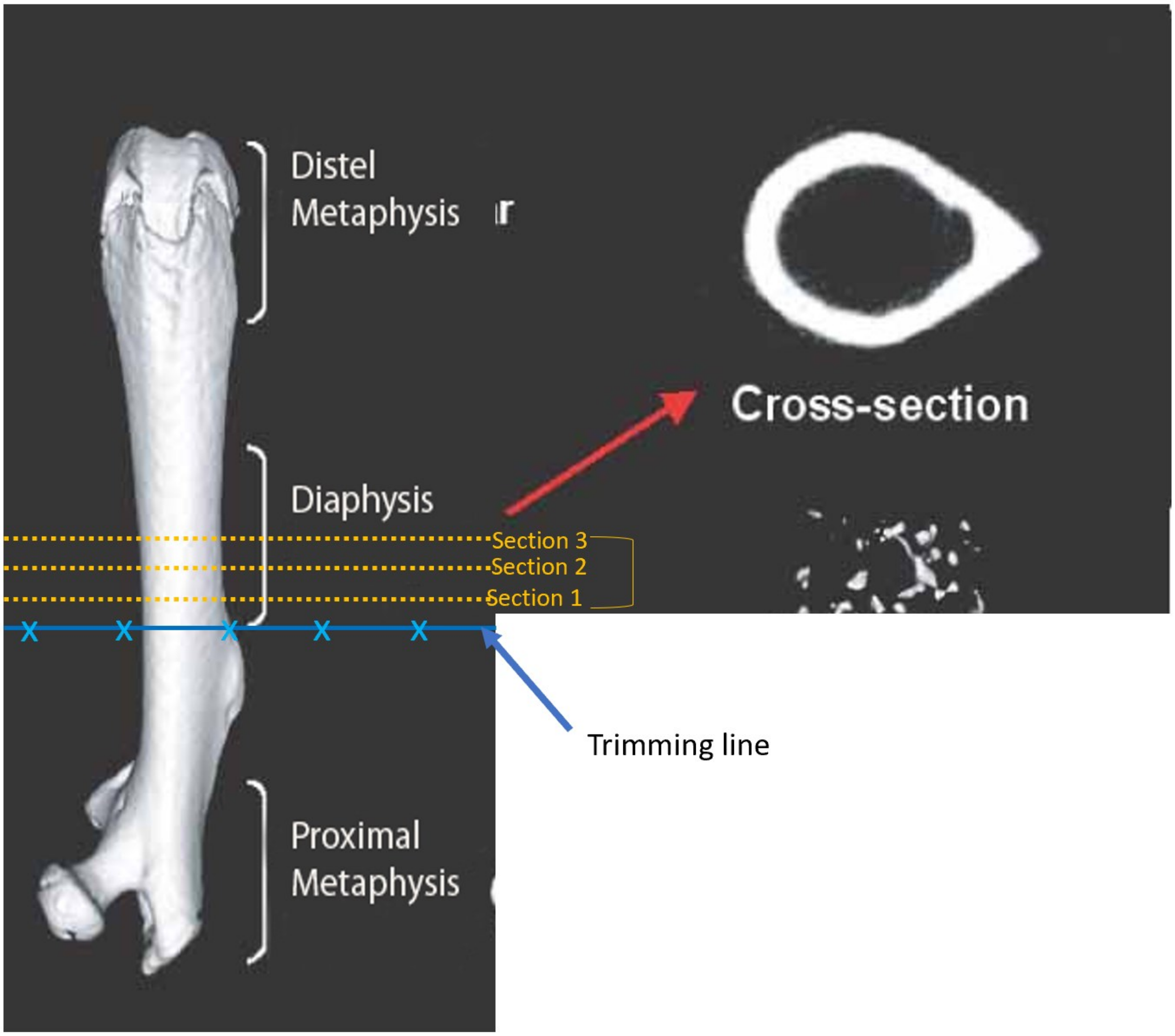

Figure 12: Three sections of the femur after the third trochanter were taken which have a cross-sectional area similar to what is shown.

The sections were ground down and polished with 1200, 800, and 600 grit sandpaper until the thickness was approximately 100µm. They were then stained with FITC dye, which permeates through and labels the bone lacunocanalicular network. 0.2 g of Fluorescein

Isothiocyanate Isomer I (Sigma, F7250) was mixed with 20 ml EtOH to prepare a 1% w/v Fluorescein Isothiocyanate (FITC) dye solution. The specimens were transferred through a graded alcohol series of 70%, 95%, and 100% EtOH, respectively, each for five minutes. The sample was then stained with 1% FITC dye for four hours with gentle shaking.

The solution was taken out and sections were air dried overnight in a dark place. The last step before confocal microscopy was to coverslip mount the samples (Platinum Line Cover Glass 24*40 #1.5) with permount just prior to imaging.

2.2.1.1 Confocal Microscopy

Confocal microscopy was performed using a Leica TCS SP5 II Laser Scanning Confocal Lower power images were collected at 5x and 20x to view the overall bone structure. For imaging of the lacunocanalicular system, detailed image stacks were collected using the100x oil immersion lens. According to the excitation and emission maxima of the FITC dye, which is shown in Figure 13, the 488 nm laser was used for excitation.

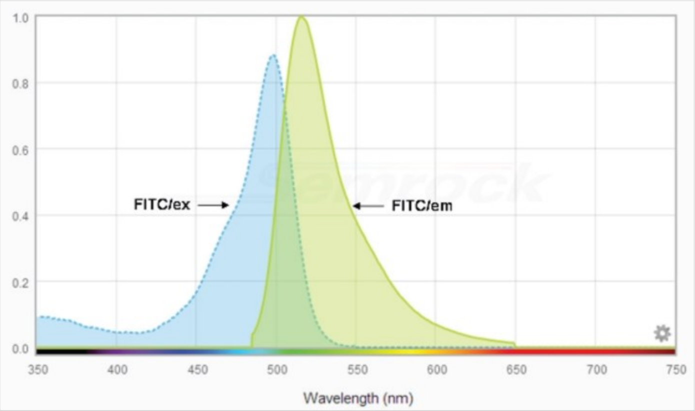

Figure 13: Excitation and Emission range for FITC dye identified for the confocal microscopy

Employing image collection techniques such as oversampling and line averaging increases the accuracy and resolution of the images. 400 z-slices were collected with the step size of 2.27 µm and voxel size of 0.0891 x 0.0891 x 0.1259 μ^3. Figure 14 depicts the transverse sections from the aged bone imaged with the 5x, 20x, and 100x objectives. The low power (5x) image shows the entire cross-section of the femur in which three regions were chosen as imaging fields. The 100x image stacks were used for computer modeling of the LCN.

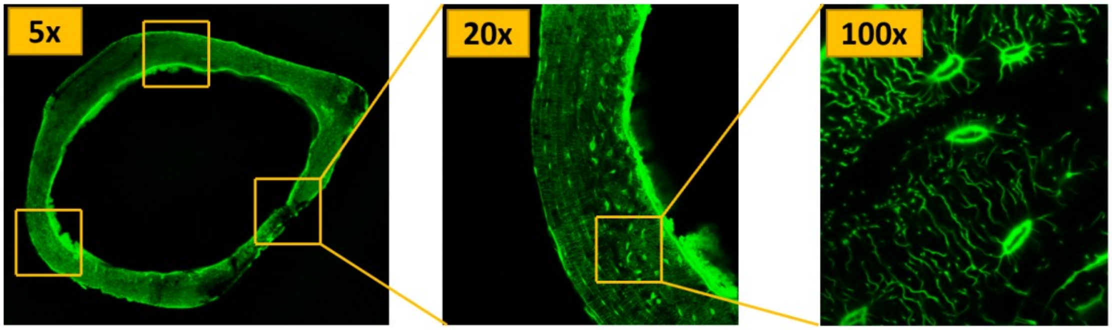

Figure 14: 5x, 20x, and 100x resolution of transverse sections of aged bone section.

2.2.2 Computer Modeling

2.2.2.1 MIMICS Innovation Suite® Software

The 100x image stacks were opened in ImageJ software to generate z-stacks with .tif format for the modeling. The z-stacks were imported into the MIMICS Innovation Suite® to construct a mask of the LCN after defining the image orientation as shown in Figure 15. It should be noted the left and right were selected in opposite to have the correct orientation. The original image from 5-month-old mouse (young mouse) was thresholded between 17,000 to 46,701 Hounsfield units, 4-month-old mouse was thresholded between 30,012 to 45,677 and the threshold for the aged mouse was between 15,000 to 46,701 Hounsfield units to most closely resemble the LCN. Thresholding helped to adjust the pixel intensity limits for inclusion in a mask.

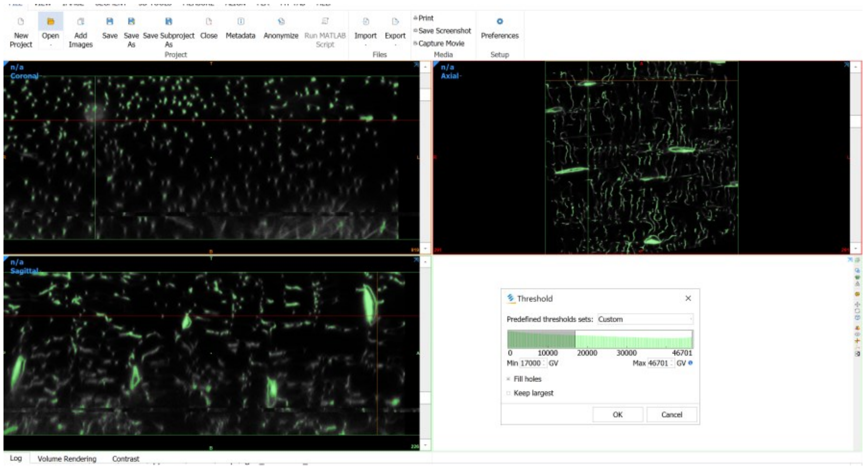

Threshold

Predefined thresholds sets: Custom

0 10000 20000 30000 46701

Min 17000 GV Max 46701 GV

☑ Fill holes

☐ Keep largest

OK Cancel

Figure 15: Thresholding the LCN to generate a surface model of lacunocanalicular region in Mimics software

One lacuna with its canaliculi was cropped from the stack to generate the CFD model of the osteocyte enclosed in an imaginary cube. Figure 16 shows the region of interest which was chosen around the lacuna using the crop mask operation. The cube was defined to capture all the canaliculi around the lacuna and keep the vertical length equal to 130 micrometers for both young and aged models. The length and width of the models depended on the size of the osteocyte and was different for the models.

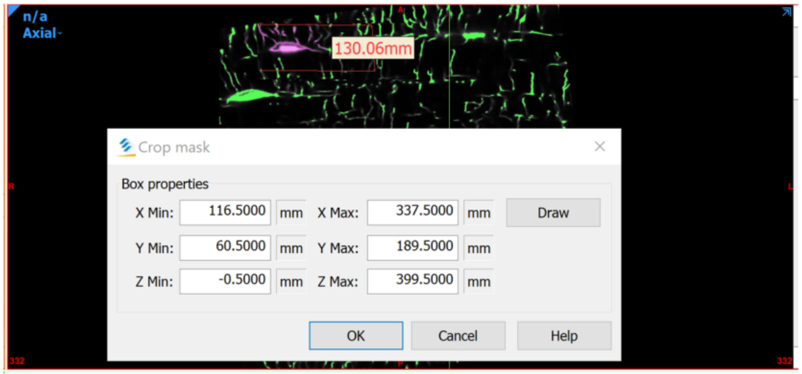

Crop mask

Box properties

X Min: 116.5000 mm X Max: 337.5000 mm

Y Min: 60.5000 mm Y Max: 189.5000 mm

Z Min: -0.5000 mm Z Max: 399.5000 mm

Draw

OK Cancel Help

Figure 16: One lacuna with its canaliculi were selected from the LCN using the Crop Mask operation

To remove all the noise and despeckle from the model, a region grow operation was performed to have a uniform lacunocanalicular region. Figure 17 shows how the quality of the initial 3D model which exists out of multiple (disconnected) parts was improved using region grow. Therefore, a uniform lacuna with connected canaliculi was obtained. The lacunocanalicular mask was converted into an object using the Calculate Part operation in MIMICS. The unique technique to build an osteocyte with dendrites involved reducing the lacunocanalicular network volume using a smoothing operation. This operation was performed several times to reach the desired dimensions. The dendrite diameter ranged from 60 to 200 nm. Figure 17 shows the Region Grow and Smoothing techniques performed on the osteocyte models.

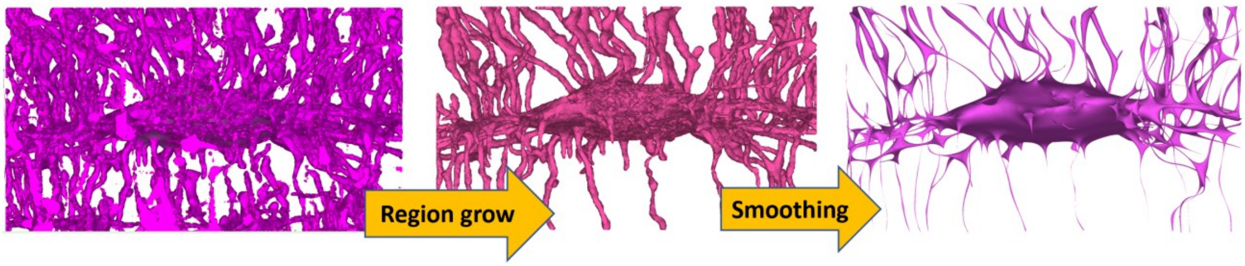

Figure 17: Region grow operation removed the noise to obtain a single part. Smoothing operation was performed to reduce the size of the lacunocanalicular network to attain osteocyte with dendrites

The last step in MIMICS was exporting the objects as STL format files. Two layers of the lacunocanalicular network and osteocyte dendritic membranes were then imported into 3-Matic software to generate a volume mesh.

2.2.2.2 3-Matic Software

After importing the parts into the 3-Matic software, some operations were performed in Fix tool to locate mesh problems and geometrical errors. The geometry status was checked using the Fix Wizard operation and an Auto fix was conducted to remove inverted normal rectangles and bad edges. The overlapping triangles could not be fixed with Auto-fix and needed to be replaced with defining new ones or using the Fill Hole Normal operation. Filter sharp triangles, filter small edges, and filter smalls shells also repaired the other geometrical issues. Then, an adaptive re-mesh was performed before generating a volume mesh.

Two surfaces of the lacunocanalicular network and osteocyte dendritic membranes were combined into one surface (lacunocanalicular space) that belongs to both parts by creating a non-manifold assembly. Figure 18 depicts the lacunocanalicular space generated by subtracting the osteocyte-dendrites from the lacunocanalicular network.

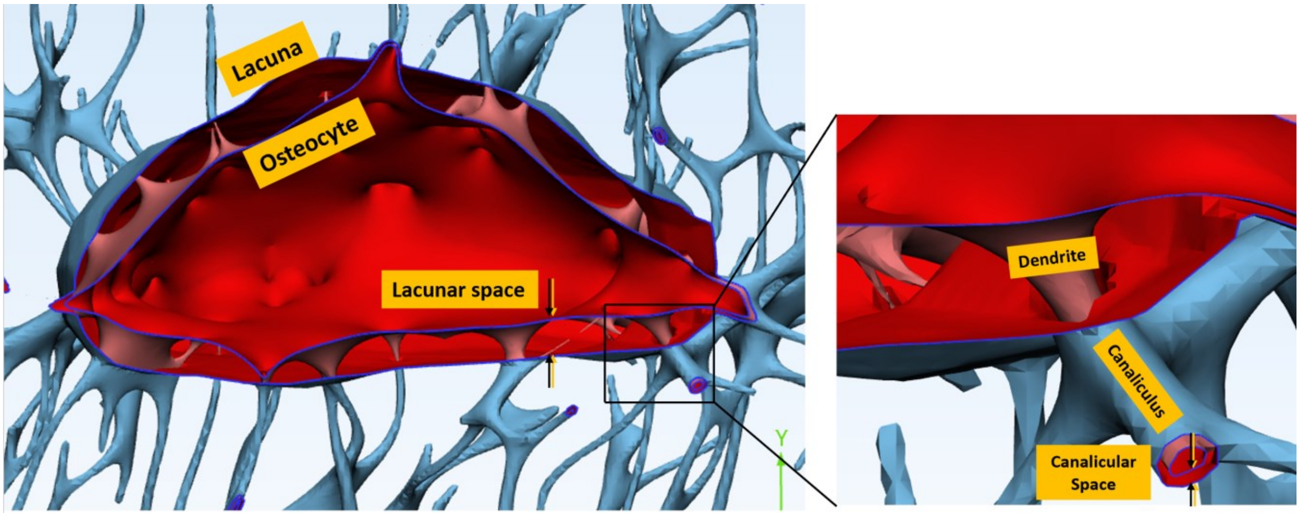

Figure 18: cross-sectional 3D view of the young osteocyte model showing modeling of the osteocyte cell membrane, lacunar wall and lacunar fluid space. The enlarged region shows modeling of the canalicular fluid space around the dendrite, where the fluid flows into or out of the cell.

A volumetric model of the lacunocanalicular space was created using the remesh operation. The final step in 3-Matic software was to export the pericellular space volume related to young and aged osteocytes to an STL format file to be imported into ANSYS software for fluid analysis. The object scale can also be adjusted in the export section as shown in Figure 19.

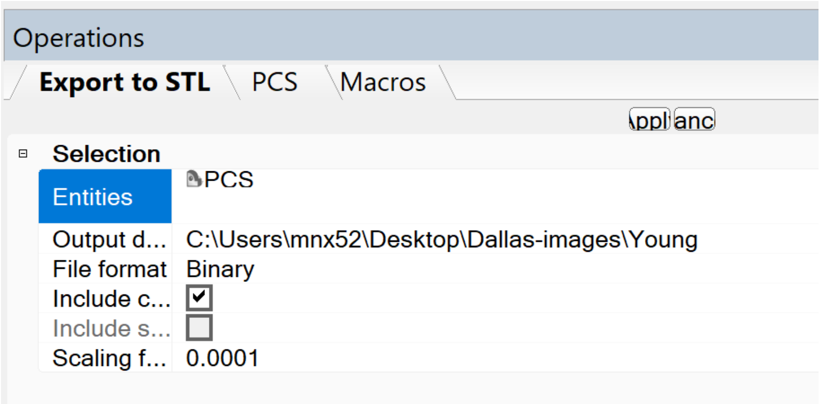

Selection

Entities: PCS

Output d...: C:\Users\mnx52\Desktop\Dallas-images\Young

File format: Binary

Include c...: ☑

Include s...: ☐

Scaling f...: 0.0001

Figure 19: Exporting the osteocyte models in 3-Matic software.

2.2.3 Confocal Image-Based Osteocyte Models of Young and Aged Mice

The computer modeling technique described in section 2.2.2 was utilized to develop 3D models of the lacunocanalicular space of the young and aged mice. Two osteocyte models of the femur of 5-month-old and 22-month-old mice were generated from the100x confocal images (described in section 2.2.1) and are shown in Figure 20. In the modeling, we kept the lacunocanalicular thickness, dendritic and canalicular diameter the same for all the models in order to only study the canalicular density due to aging.

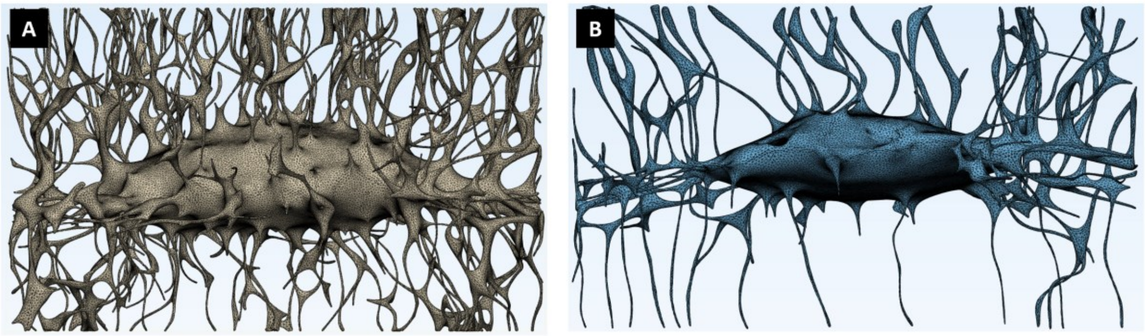

Figure 20: Confocal image-based osteocyte models of A) 5-month-old and B) 22-month-old mice developed to analyze fluid inside the lacunocanalicular space

Another osteocyte model (Figure 21) was generated from a 4-month-old mouse which was used to develop new simulated osteocyte models using geometry modification techniques which will be explained in the section 2.2.3.1.

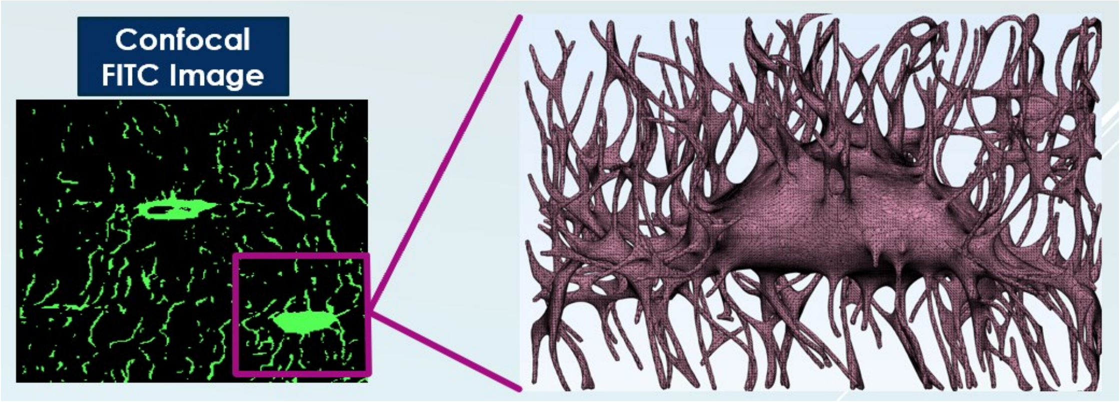

Figure 21: Confocal image-based osteocyte model of the 4-month-old mouse developed from 100X confocal image stacks.

2.2.3.1 Simulated Osteocyte Models

To study the effect of various morphological parameters such as dendrite diameter, lacunocanalicular space thickness, and canalicular density due to aging, several distinct osteocyte models were developed from one confocal image (4-month-old mouse) using a geometry modification technique. One of the benefits of this technique was to investigate the effect of each of these morphological parameters on fluid flow shear stress while the osteocyte shape was kept the same. Six new simulated models were developed from the same young mouse image. One morphology parameter was changed in each of them using geometry modification techniques in MIMICS and 3-Matic software. These models predict the effect of alteration in dendrite diameter, lacunocanalicular space thickness, and canalicular density while the osteocyte shape remained the same.

The geometry modification techniques will be explained in three parts, “decreased canalicular density”, “increasing dendritic diameter”, and “increasing lacunocanalicular thickness”. In each of them, the base model (young osteocyte) was modified to apply morphology alteration.

2.2.3.1.1 Lower Canalicular Density

Generating osteocyte models from the base model with different canalicular densities was carried out by changing the image thresholding in MIMICS software. To reduce the light intensity of the image, a lower threshold, which depends on the number of canaliculi needed to be removed, was selected to obtain a lacuna with fewer canaliculi. The advantage of the thresholding technique was that the lacuna shape and size remained the same and only the influence of canalicular density was studied. Figure 22 shows two models with lower canalicular density besides the original young osteocyte model as the base model (Model 1). Model 2 and Model 3 were named simulated middle-age and simulated aged models, respectively. The number of canaliculi in the original image related to the young osteocyte is 92 [39], whereas the Model 2 and Model 3 model with a lower threshold had 43 and 22 canaliculi, respectively. The other parameters including dendrite diameter and lacunocanalicular thickness were kept the same for them which is shown in the magnified figure at the bottom.

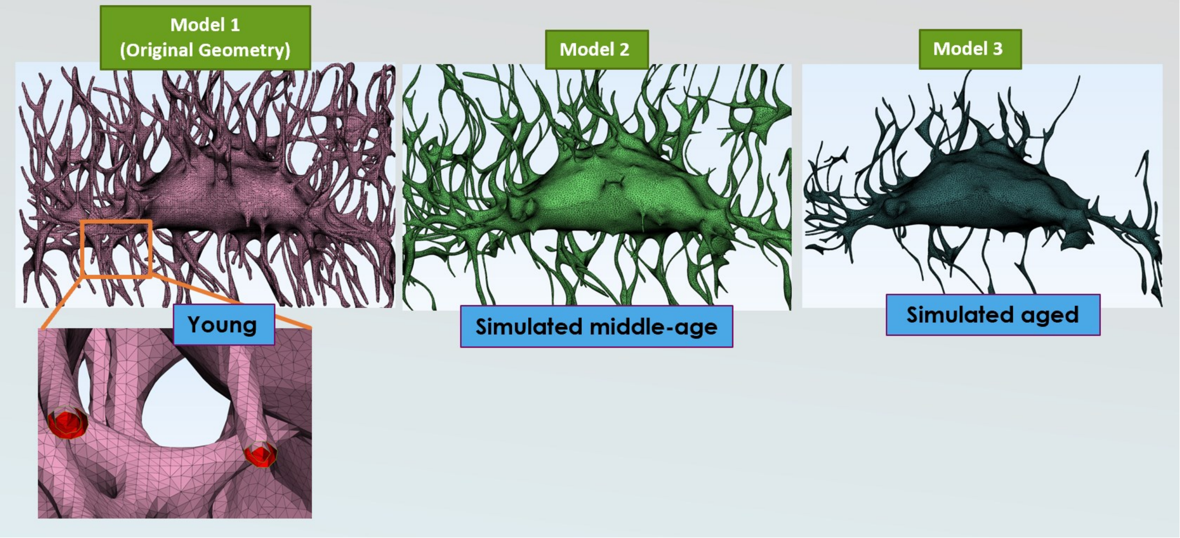

Figure 22: 4-month-old mouse (Model 1) was modified using the geometry modification technique to build Model 2 and Model 3 with a lower canalicular density. The magnified section shows the dendrite diameter and lacunocanalicular thickness which was kept the same for all of these models.

2.2.3.1.2 Increasing Dendritic Diameter

Model 4 and Model 5 were generated from the same young mouse image with the same canalicular density and lacunocanalicular space thickness as the original osteocyte model but with an increase in dendritic diameter. Larger or smaller dendritic diameter can be generated using wrapping or smoothing operations in MIMICS software. The dendrite diameter in Model 4 and Model 5 were two and four times, respectively greater than the diameter of dendrite in the original geometry.

Figure 23 depicts the dendrite diameter increase in Model 4 and Model 5 compared to dendrite diameter of the original Model 1. It can be observed that the canalicular space around the dendrites which is the path for the fluid movement is equal in all the models. As a consequence of increasing dendrite diameter, canaliculus diameter increased as well while keeping the canalicular fluid space around the dendrites the same (80 nm).

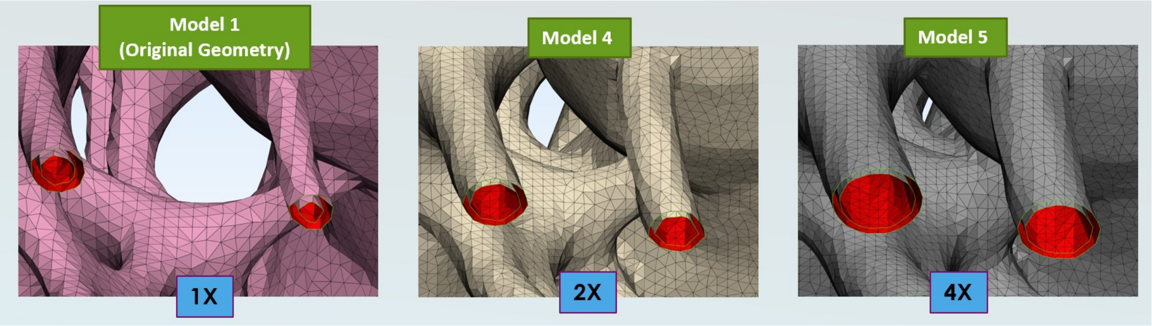

Figure 23: Model 4 and Model 5 were developed by increasing dendrite diameter to two and four times from the same young osteocyte model (Model 1)

2.2.2.2.3 Increasing Lacunocanalicular Space Thickness

Model 6 and Model 7 were developed by keeping the dendrite diameter and canalicular density the same as Model 1 but with different lacunocanalicular space thickness. The lacunocanalicular space thickness in Model 6 and Model 7 is two and four times greater than its thickness in the original model. It should be noted that the lacunocanalicular space is the space in which fluid flows around the cell and dendrites. Therefore, a greater amount of fluid can flow in such a greater space in these two models.

Figure 24 shows how the lacunocanalicular space thickness in Model 6 and Model 7 was increased two and four times compared to Model 1. Other parameters including the number of dendrites and dendrite diameter is equal for all these models.

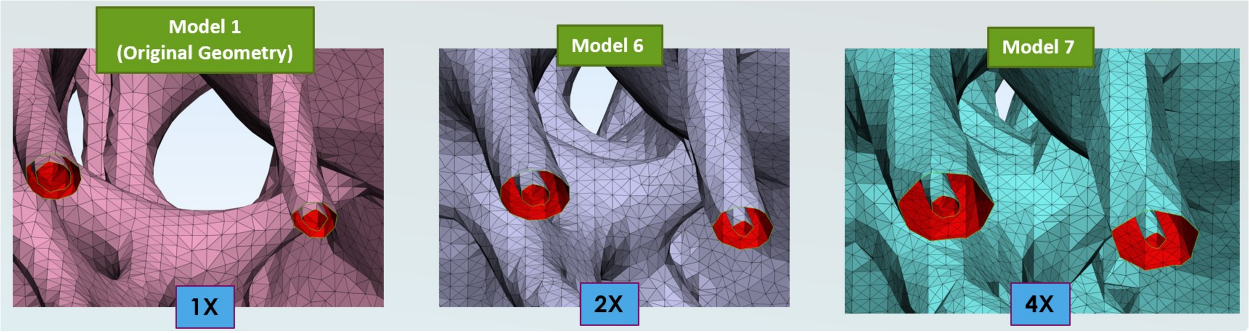

Figure 24: Model 6 and Model 7 were developed by increasing the lacunocanalicular space thickness to two and four times from the original model (Model 1)

2.3 Computational Fluid Dynamics (CFD) Analysis

After generating the volumetric osteocyte model from the confocal microscope image, it was imported into the CFX module of ANSYS Workbench software for a CFD analysis. Several steps including geometry, mesh, and setup were carried out to prepare the models for CFD analysis. Figure 25 shows the project schematic of ANSYS CFX in which the problem was defined.

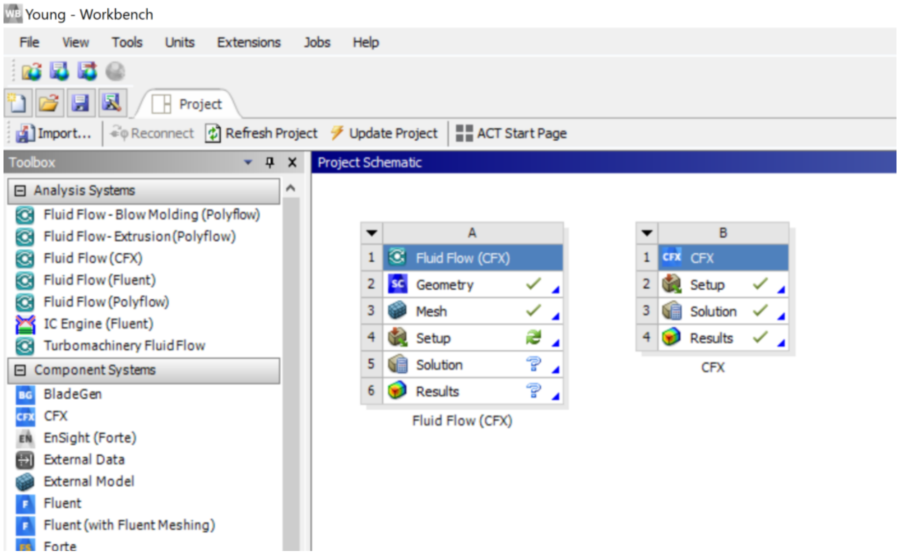

Figure 25: Project schematic of ANSYS CFX for CFD analysis

2.3.1 Geometry

The developed confocal image-based geometries were imported in the geometry section of CFX, known as ANSYS SpaceClaim. The unit dimensions were set to nanometer in the setting. Geometry appeared as two facets of lacunocanalicular network and osteocyte dendritic processes. Each of the facets was fixed to remove some geometrical errors such as intersections, sharp or overconnected edges and vertices, and detect and fixing openings or holes. Figure 26 shows two facets, the osteocyte dendritic process which is surrounded by lacunocanalicular network.

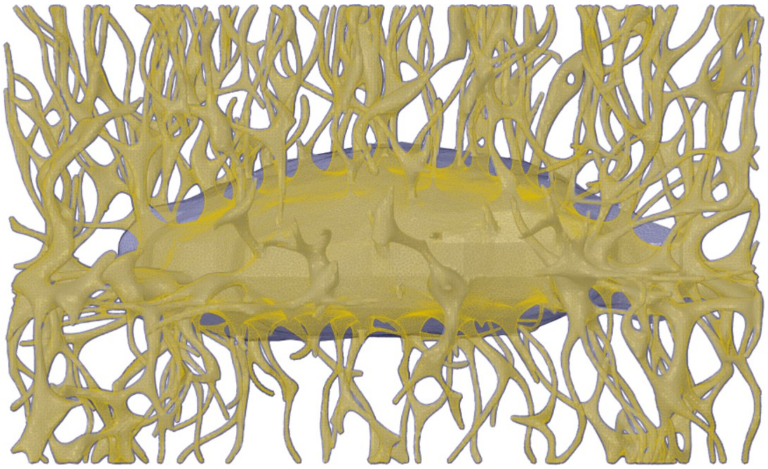

Figure 26: Geometry in ANSYS Space Claim includes the smaller facet of osteocyte dendritic processes and the bigger facet of lacunocanalicular network

The smaller facet which was osteocyte dendritic processes was subtracted from the larger facet, lacunocanalicular network to achieve a single body of lacunocanalicular space. It was then converted from facets to a solid domain without merging faces. Figure 27 shows the cross-sectional area of the young osteocyte model (4-month-old mouse) which represents the lacunocanalicular space. It is visible that the lacunar fluid space around the osteocyte is larger than the space around the dendrites. In the next steps, a fluid pressure will be defined to be inserted into these spaces around the osteocyte-dendrites.

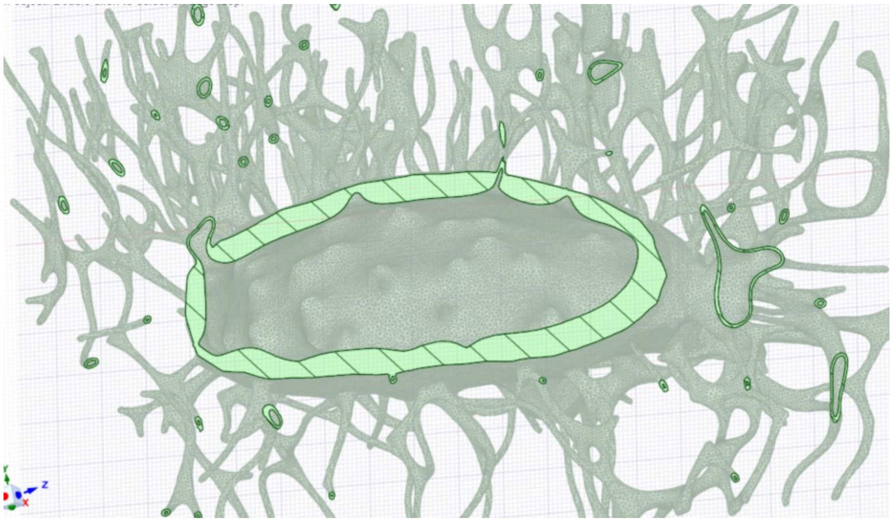

Figure 27: Cross-section area of young osteocyte model in ANSYS Space Claim

2.3.2 Mesh

The geometries were meshed with linear tetrahedral elements, using an element size of 0.06 µm. A fine mesh was chosen to have enough elements in the tiny dendritic system. For, instance, the total elements for young and simulated aged osteocytes are 10,116,847 and 5,075,600. The fluid inlets and outlets were chosen using a box select and defining several faces. The canaliculi on the top were selected as fluid inlets and the canaliculi on the other five faces were selected as fluid outlets. Figure 28 shows the details of the project outline which includes the geometry, mesh, and two inlet and outlet name selections.

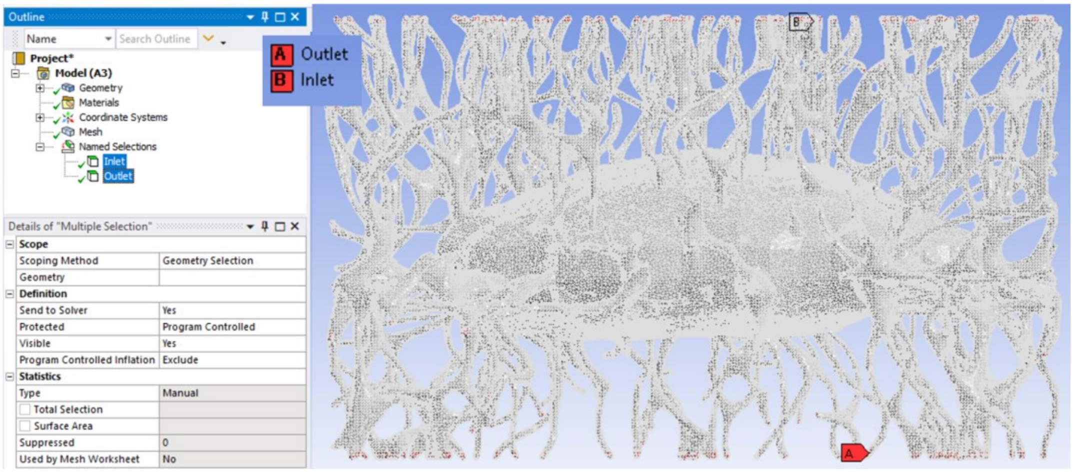

Scope	
Scoping Method	Geometry Selection
Geometry	
Definition	
Send to Solver	Yes
Protected	Program Controlled
Visible	Yes
Program Controlled Inflation	Exclude
Statistics	
Type	Manual
☐ Total Selection	
☐ Surface Area	
Suppressed	0
Used by Mesh Worksheet	No

Figure 28: Project outline in defining name selection in ANSYS CFX

It is worth noting that a mesh independence study was done to obtain accurate results. By reducing the number of elements to 10,116,847 and 5,075,600 for the young and aged osteocyte models, respectively, FFSS results does not change. The last step in Space Claim was to export the mesh as a fluent file format as it loads faster in the setup owing to the complicated geometry of osteocytes.

2.3.3 Setup

The generated fluent mesh was then imported in the setup section of CFX. Using insert boundary option, two boundary conditions of inlets and outlets were defined for the faces preselected as inlets/outlets. To imitate physiological conditions, a fluid inlet pressure of 300 Pa was exerted on the inlets and outlets had a pressure of 0 Pa [40, 41]. The remaining surfaces were treated as walls with a no-slip condition in that fluid has zero velocity at the interface of walls. Figure 29 shows all the inlets and outlets which were the canaliculi on the six faces of the osteocyte model.

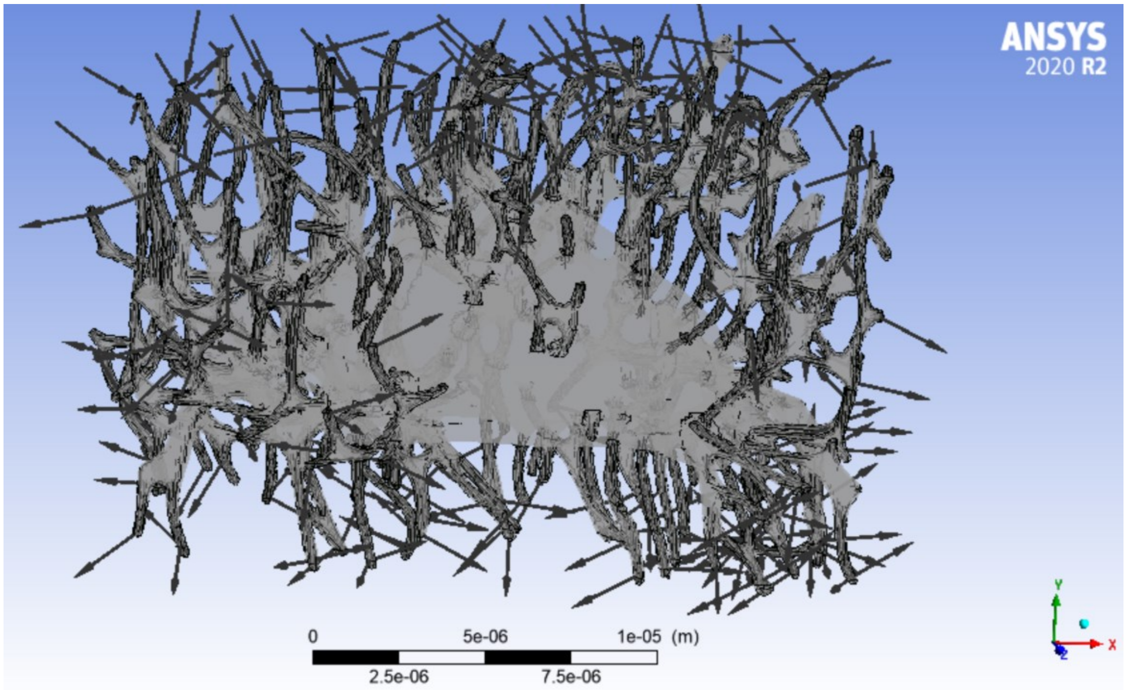

Figure 29: Defined fluid inlets and outlets to the cell as boundary conditions of osteocyte model

Fluid flows from the inlets around the dendrites and osteocyte cell body and exits from the other canaliculi were assigned as outlets. It should be also noted that the fluid inlets considered were on the top side of the imaginary cube and canaliculi on the other five faces were outlets as shown in Figure 30.

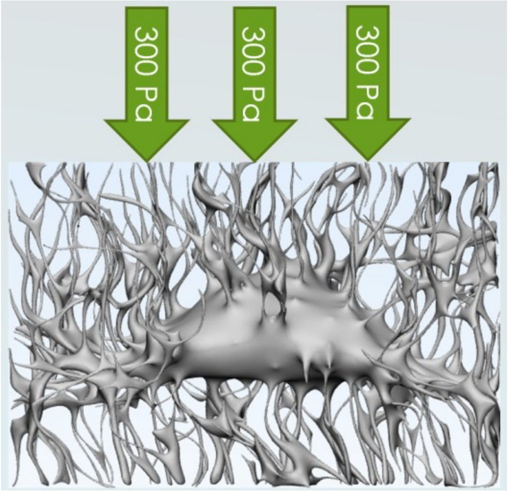

Figure 30: Fluid inserts to the cell from the inlets, canaliculi on the top side, and exits from other canaliculi on the other sides of the model which are outlets

The interstitial laminar fluid was treated as water [23] and was chosen from the material library. The heat transfer, combustion, and thermal radiation sections were set to none as there was not any heat transfer defined in the problem. The turbulence mode also changed to none as the fluid characteristic in the lacunocanalicular network is similar to a laminar fluid [23]. In the solver control, maximum 300 iterations and a residual target of 1e-12 was set for the problem.

The software ran using double precision and maximum number of 6 cores of the system parallel together (Inlet MPI Local Parallel). Mass and momentum were monitored until residuals drop and become constant (Figure 31). After solution convergence, FFSS data were measured in the CFD-post section of ANSYS CFX.

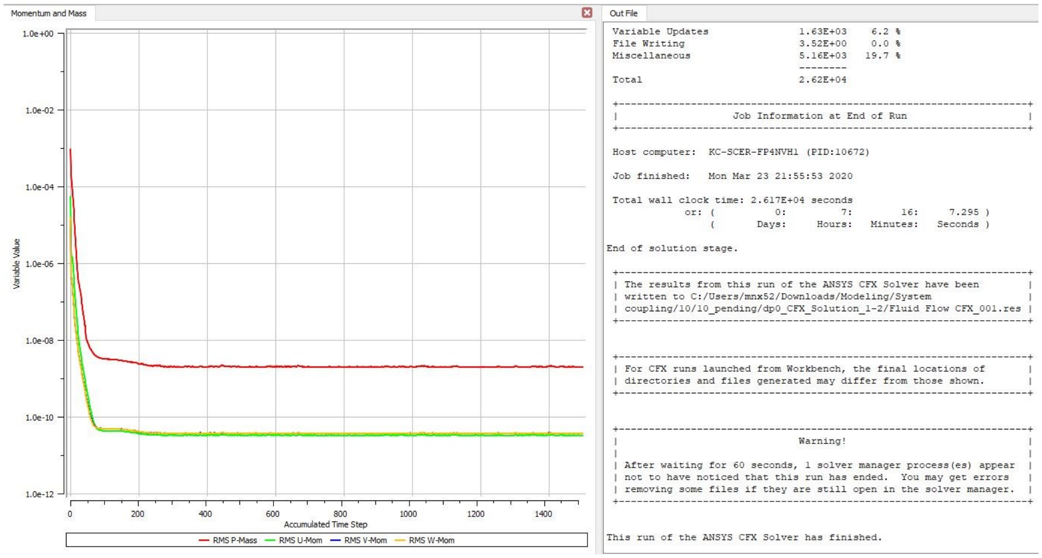

```
 Variable Updates               1.63E+03    6.2 %
 File Writing                   3.52E+00    0.0 %
 Miscellaneous                  5.16E+03   19.7 %
                                --------
 Total                          2.62E+04

 +--------------------------------------------------------------------+
 |                 Job Information at End of Run                      |
 +--------------------------------------------------------------------+

 Host computer:  KC-SCER-FP4NVH1 (PID:10672)

 Job finished:   Mon Mar 23 21:55:53 2020

 Total wall clock time: 2.617E+04 seconds
             or: (          0:          7:         16:      7.295 )
                 (       Days:      Hours:   Minutes:    Seconds )

End of solution stage.

 +--------------------------------------------------------------------+
 | The results from this run of the ANSYS CFX Solver have been        |
 | written to C:/Users/mnx52/Downloads/Modeling/System                |
 | coupling/10/10_pending/dp0_CFX_Solution_1-2/Fluid Flow CFX_001.res |
 +--------------------------------------------------------------------+


 +--------------------------------------------------------------------+
 | For CFX runs launched from Workbench, the final locations of       |
 | directories and files generated may differ from those shown.       |
 +--------------------------------------------------------------------+


 +--------------------------------------------------------------------+
 |                              Warning!                              |
 |                                                                    |
 | After waiting for 60 seconds, 1 solver manager process(es) appear  |
 | not to have noticed that this run has ended.  You may get errors   |
 | removing some files if they are still open in the solver manager.  |
 +--------------------------------------------------------------------+


This run of the ANSYS CFX Solver has finished.
```

Figure 31: Mass and momentum residuals drops after solution convergence

2.3.4 Post Processing

To depict FFSS experienced by osteocytes and dendrites, a new contour was inserted in the results section of ANSYS CFX. Variable was chosen as wall shear on the osteocyte dendritic membranes as the domain and the FFSS contour was created. It should be noted that to better show high FFSS on dendritic membranes, the range of FFSS can be set to User Specified to modify min/max values of FFSS.

Velocity streamlines were also inserted for the lacunocanalicular domain starting from the inlets. Sampling was equally spaced, and number of points was selected as 2500. There is an animation section in CFX which accurately displays in 3D how the fluid particles flow inside the lacunocanalicular spaces using the velocity streamline graph.

Function calculator in CFX was a valuable tool to analyze the magnitude of FFSS or velocity based on geometrical parameters, especially where there are various osteocyte models (e.g. young vs aged). The volume and surface area of lacunocanalicular space could be measured as geometrical parameters along with maximum, minimum, or average FFSS values.

To depict strain results, a new contour was inserted in the results section of ANSYS CFX. In the FSI problem, since the Structural and CFX modules were connected, the Structural module results were obtained in the CFX section. The default domain was selected as the lacunocanalicular region to visualize the strain magnitudes.

3 CHAPTER 3: RESULTS

This chapter includes the data generated by following the methods described in Chapter 2. The bone strain experienced by the osteocytes and shear stress response on the cell membrane and dendritic processes was calculated for idealized and confocal-based osteocyte models. The data presented in this chapter shows the comparison of the stress/strain values captured from different methods of developing osteocytes. It first shows the differences observed in shear stress and bone strain response in the idealized geometry models with alteration in the number of fluid inlets, load direction, canalicular density and then presents the difference in shear stress values for the confocal image-based models for young and aged osteocytes and also, for the simulated models with changing lacunocanalicular space thickness, dendrite diameter, and canalicular density. The fluid flow shear stresses experienced by osteocyte is presented based on the lacunocanalicular volume and surface area to find out the correlation between the osteocyte fluid flow shear stress with the structure of the lacunocanalicular network, which will be discussed in the next chapter.

3.1 Idealized Geometry

In all four models, because the canalicular space surrounding the dendrites is roughly nine times smaller than that surrounding the osteocyte, dendrites encounter higher maximum shear stresses on the walls than the cell membrane: consistent with previous studies [23, 42, 43]. Dendrites have a maximum FFSS of approximately 3-5.3 Pa. Junctions of the dendrites and the cell body have an FFSS of approximately 0.6-0.9 Pa if those dendrites are fluid inlets, while then the FFSS concentration at the rest of the cell membrane is even smaller 0.006-0.029 Pa. The effect of the following parameters on FFSS was determined considering differences in morphology and loading condition of four models. Figure 32 depicts the shear stress distribution on the cell and dendrites within four idealized models.

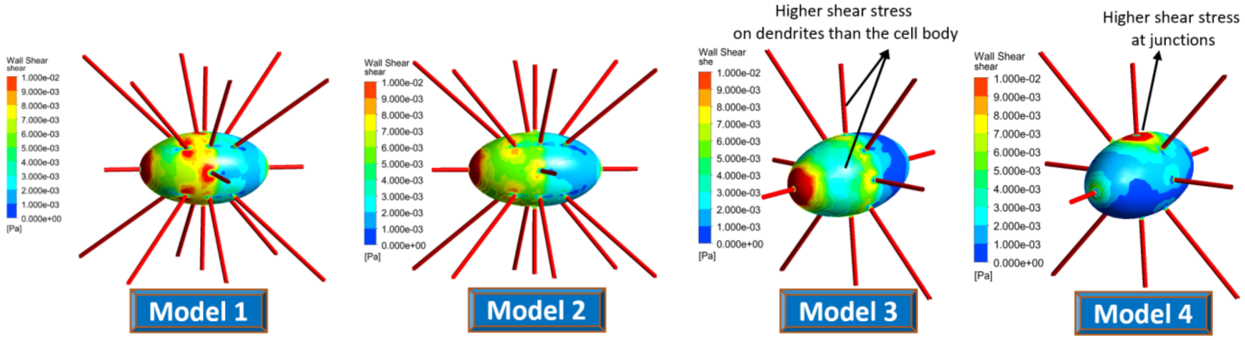

Figure 32: FFSS contours of four osteocyte models with idealized geometries: 18-dendrites models with five and one fluid inlet (Model 1 and Model 2) with a left load, 10-dendrites models with one fluid inlet with an applied left load (Model 3) and top load (Model 4)

3.1.1 Effect of Inlet Number on FFSS

In order to understand the relationship between flow and FFSS we built idealized computer models with either ten or eighteen dendrites to test the effects of one vs five inlets with regard to canalicular density. With comparison of Model 1, Model 2 and Model 3, we investigated the responsiveness of osteocytes in terms of shear stress to mechanical loading to determine if the osteocytes with higher canalicular density or/and number of fluid inlets produce higher shear stresses.

The minimum shear stress threshold required to deform the osteocyte cell membrane has been postulated to be 0.8 Pa [9, 15], so we determined the number of dendrites with FFSS values greater than 0.8 Pa (shown in Table 1 and Figure 33). In Model 1 with five fluid inlets nine of eighteen dendrites experienced shear stresses greater than 0.8 Pa (Table 1 and Figure 33). In Model 2, with only one inlet, only two of eighteen dendrites reached 0.8 Pa of shear stress. In Model 3, which has one fluid inlet and ten dendrites, two out of ten dendrites experienced FFSS values above 0.8 Pa. The incorporation of four additional inlets in Model 1, which results in higher volumetric flow rates, increases the FFSS in almost all dendrites (Table 1 and Figure 33).

3.1.2 Effect of Load Direction on FFSS

We next compared load direction relative to FFSS from a single inlet. Figure 33 displays the maximum FFSS for the idealized models. Models 1, 2, and 3, in which load was applied on the left side (parallel to the long axis of the lacuna), have a maximum FFSS of 4.44 Pa, 5.0 Pa, and 5.3 Pa, respectively. In contrast, the maximum FFSS in Model 4 only reached 3.07 Pa.

As shown in Model 4 (Table 1 and Figure 33), only one of the ten dendrites reached the stress threshold of 0.8 Pa. By comparing Model 4 to Model 3, where both have the same number of dendrites and fluid inlets but a different load direction, we observed higher FFSS when the flow direction is aligned along the major axis in all dendrites. In Model 3, dendrites one and ten are aligned with the load direction and show the highest FFSS (both reach to 0.8 Pa). In Model 4, dendrites three and seven are aligned with the load direction and show the highest FFSS (only one of them reaches to 0.8Pa).

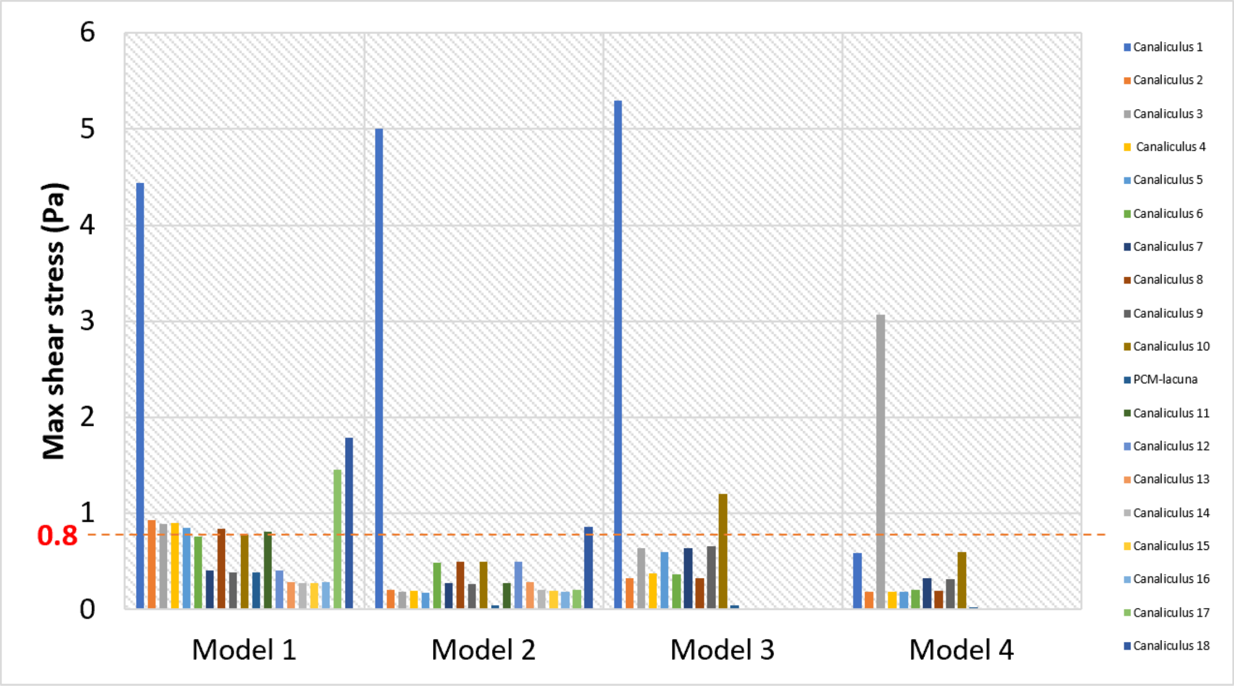

Figure 33: Comparison of experienced maximum FFSS in four models

Table 1: Number of dendrites in each Model that experience a FFSS ≥ 0.8 Pa

	Number of dendrites	Number of fluid inlets to the cell	Dendrites Experiencing FFSS > 0.8 Pa
Model 1	18	5	9/18
Model 2	18	1	2/18
Model 3	10	1	2/10
Model 4	10	1	1/10

3.1.3 Effect of Dendrite Number and Load Direction on Strain Distribution

As direct mechanical deformation (strain) on the osteocyte may also contribute to load related responses, we next compared the mechanical strain distribution in each of the four models. We observed that maximum strains occur at the junction of the canaliculi to the lacuna, especially where those canaliculi are aligned with the applied mechanical load. Figure 34 shows the strain distribution in Model 3. Since the load was applied from the left side, the two left and right canaliculi experienced the highest compressive strain.

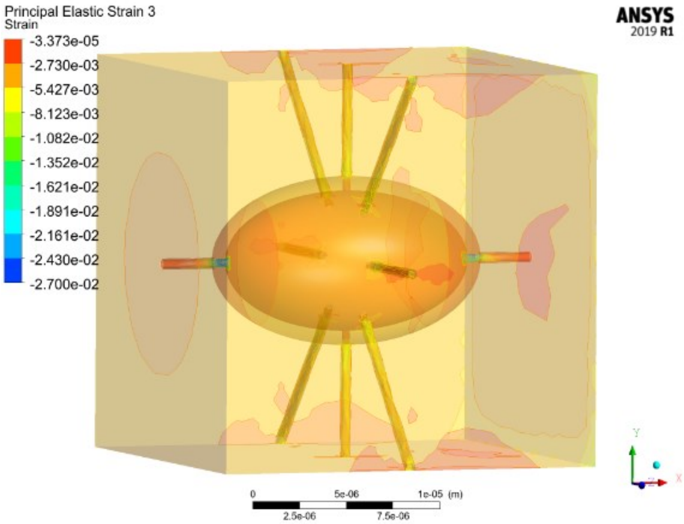

Figure 34: Strain distribution of Model 3 in the bone matrix and lacunocanalicular region

Figure 35 illustrates the specific regions of the lacunocanalicular walls in the four models filtered with compressive strains over 5,000 με, the minimum strain to cause some biochemical response in osteocytes according to cell culture studies [12, 13]. The rectangular frame in each model shows the regions of bone with strains over 5,000 με. These high strain regions, which constitute fewer than 2% of the surface area of each osteocyte model (Table 2), are primarily localized to the canaliculi and a small region of the lacuna. Each model exhibits a distinct pattern of mechanical strain, altered when the loading direction is changed (Figure 35). For example, Model 1, Model 2, and Model 3 have the same strain pattern as they have the same loading direction (from left to right) but changing the load direction (top to bottom) in Model 4, changes the strain pattern to a ring shape around the lacuna.

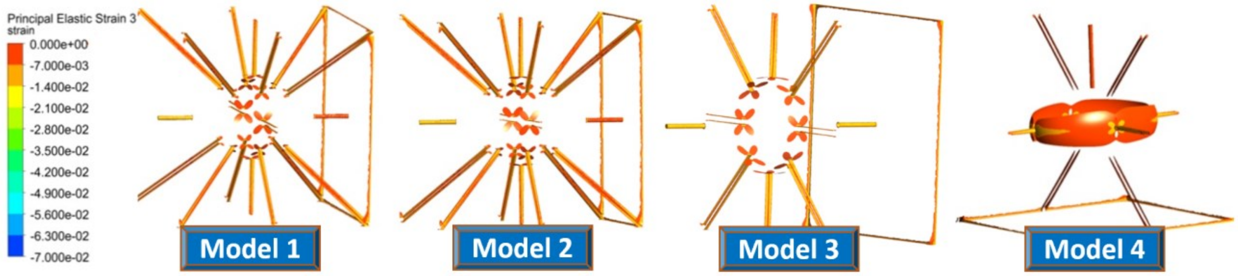

Figure 35: Regions which experienced strains greater than 5,000 με in the four idealized Models. The highest strains are experienced in the regions shaded red in the 4 Models.

Table 2 shows the volume percentage of each model in different strain ranges. In all osteocyte models, more than 80% of the model experiences strain less than 1,000 με. In the 18-dendrite models, 0.12% of the entire model have resultant strains more than 10,000 με, the strain postulated to trigger a significant osteogenic response [12, 13]. Nevertheless, 0.11% and 0.08% of the other models experience high strain magnitudes.

Table 2: Volume percentage of each model that experiences different ranges of strains magnitudes

	Volume Percentage			
	strains< 1000 μƐ	1000 μƐ <strains< 5000 μƐ	5000 μƐ <strains> 10000 μƐ	strains> 10000 μƐ
Model 1	81.15	17.00	1.73	0.12
Model 2	81.30	16.85	1.73	0.12
Model 3	84.63	14.44	0.82	0.11
Model 4	84.60	14.14	1.18	0.08

3.2 Confocal Image-Derived Osteocyte Models

To simulate the effects of aging on the LCN [17], we developed a more realistic model of an osteocyte and its dendritic processes as it resides within bone from confocal image sets (Figure 20). CFD modeling showed concentrations of FFSS on the dendritic walls, and at the inlet and outlet points. CFD modeling showed concentrations of FFSS on the dendritic walls, and at the inlet and outlet points. We compared the maximum and average FFSS magnitude on osteocyte and dendrites using CFD-post techniques in ANSYS.

3.2.1 Young and Aged Models

3.2.1.1 FFSS Results

The average FFSS on the cell membrane and dendrites in the young osteocyte model (5-month-old mouse) was 0.3 Pa. With aging (22-month-old mouse), the osteocyte experienced a lower amounts of average shear stress which was about 0.19 Pa. The maximum FFSS on the cell membrane and dendritic processes in the young and aged osteocyte models was 4.85 Pa and 6.5 Pa. The surface area of young osteocyte was 3102.3 μm^2, while the aged osteocyte model had a 2.2 times smaller surface (1372.7 μm^2). The total lacunocanalicular fluid space for the young and aged models was 333.6 μm^3 and 229.4 μm^3, respectively. Figure 36 depicts the fluid shear stress experienced by the osteocyte cell membrane and dendritic processes for young and aged osteocytes.

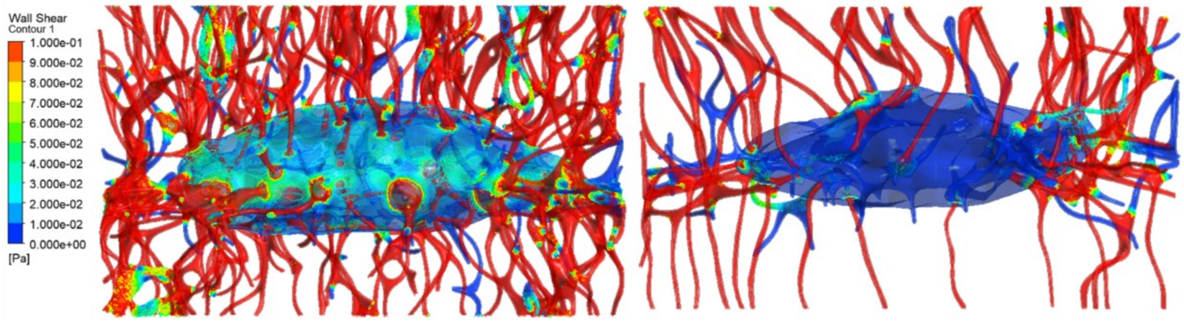

Figure 36: Contour plots of FFSS in young and aged osteocyte models based on confocal image stacks

3.2.1.2 Velocity Streamlines

Young (5-month-old) and aged (22-month-old) osteocytes experience different ranges of velocity values inside the lacunocanalicular space. Canaliculi have higher velocities compared to the lacuna. The maximum velocity in young and aged osteocytes is 2.45 e-4 m/s and 7.7 e-4 m/s. The young osteocyte model has an average velocity of 9.58 μm/s while with aging, the average velocity decreases to 5.78 μm/s.

Figure 37 and figure 38 depict the velocity streamlines in the lacunocanalicular space around the cell and cell processes for the young and aged osteocyte, respectively. The velocity of fluid decreases in the lacuna as the space around the cell is much greater than the space around the dendrites.

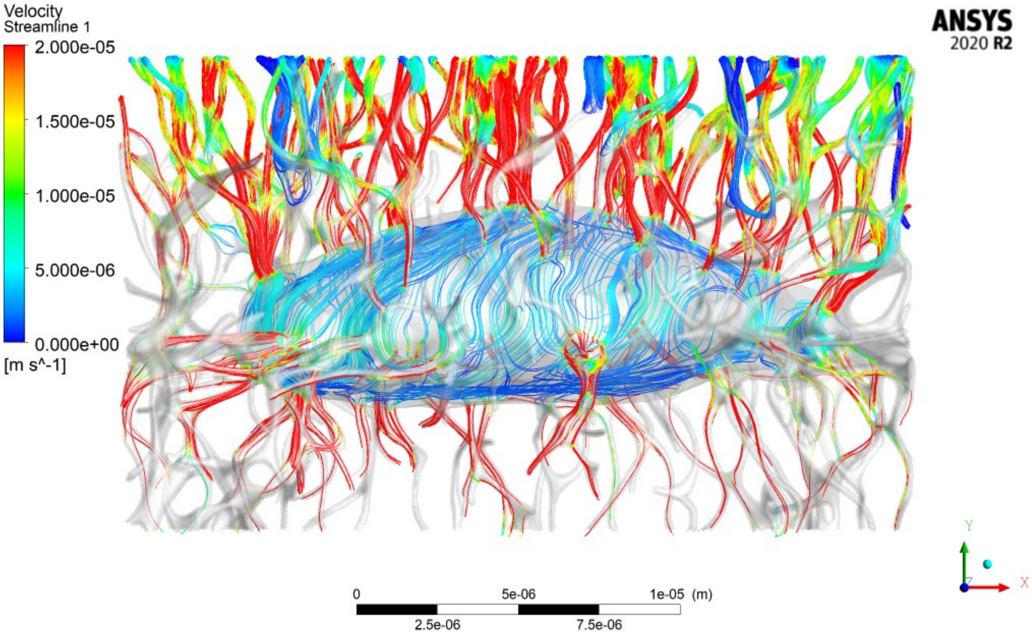

Figure 37: Velocity streamlines in the lacunocanalicular space in young osteocyte (5-month-old) mouse

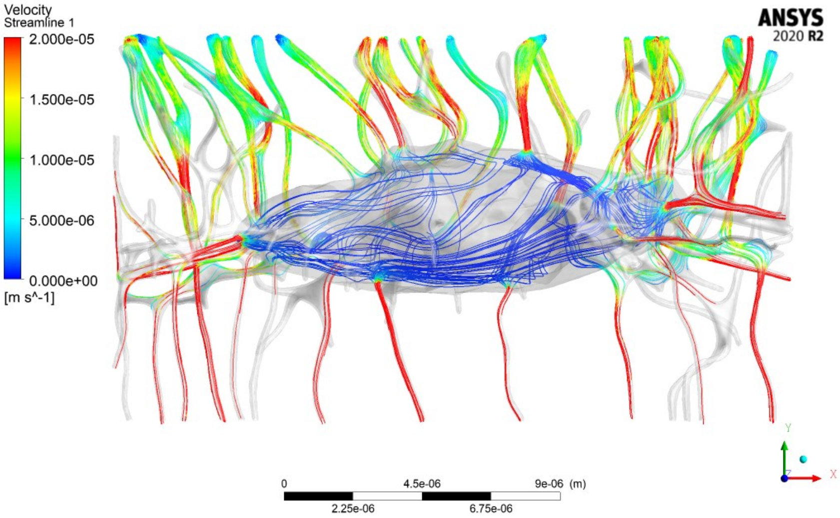

Figure 38: Velocity streamlines in the lacunocanalicular space in aged osteocyte (22-month-old) mouse

The velocity profile also was measured for the other young osteocyte model generated from the 4-month-old mouse (Model 1). Figure 39A demonstrates velocity streamlines inside the lacunocanalicular system. Canaliculi, particularly the upper ones, have higher velocities than the lacuna because they are fluid inlets. The canaliculi with the highest velocities have a red color. The peak velocity (2.69 e-4 m/s) is an order of magnitude greater than the average velocity of the entire area (1.07 e-5 m/s). Fluid velocity profile varies depending on the microstructural configuration of the LCN in this realistic osteocyte model, such as branching, canalicular junctions, and narrow channels. Figure 39B indicates that canalicular branches alter the fluid flow profile. Canalicular junctions experience lower velocity values, as shown in Figure 39C. As seen in Figure 39D, fluid has higher fluid velocities in narrow channels due to their smaller cross-section area.

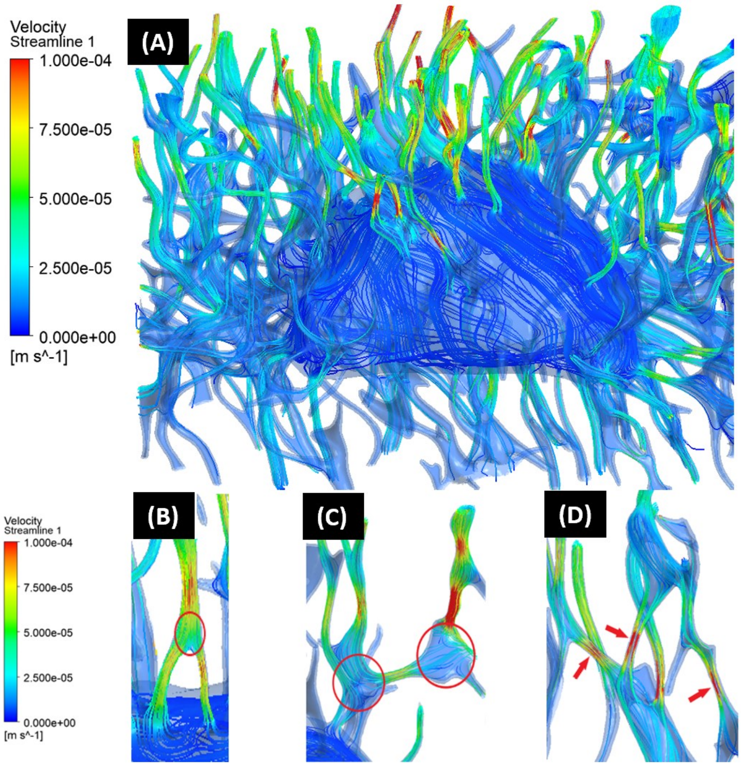

Figure 39: A) Velocity streamlines in the realistic young osteocyte model inside the lacunar and canalicular fluid spaces surrounding the cell and dendrites. Alteration of the fluid velocity profile in image-derived models due to tortuosity of the canaliculi is presented in B) Canalicular branches, C) Canalicular junctions, D) Narrow channels

Figure 40 illustrates velocity streamlines within the lacunocanalicular space in a top view of the young osteocyte model. Half of the osteocyte is shown using a cut plane to observe clearly the canaliculi connected to the lacuna. Most canaliculi experience higher velocities at the locations where canaliculi connect to the lacuna.

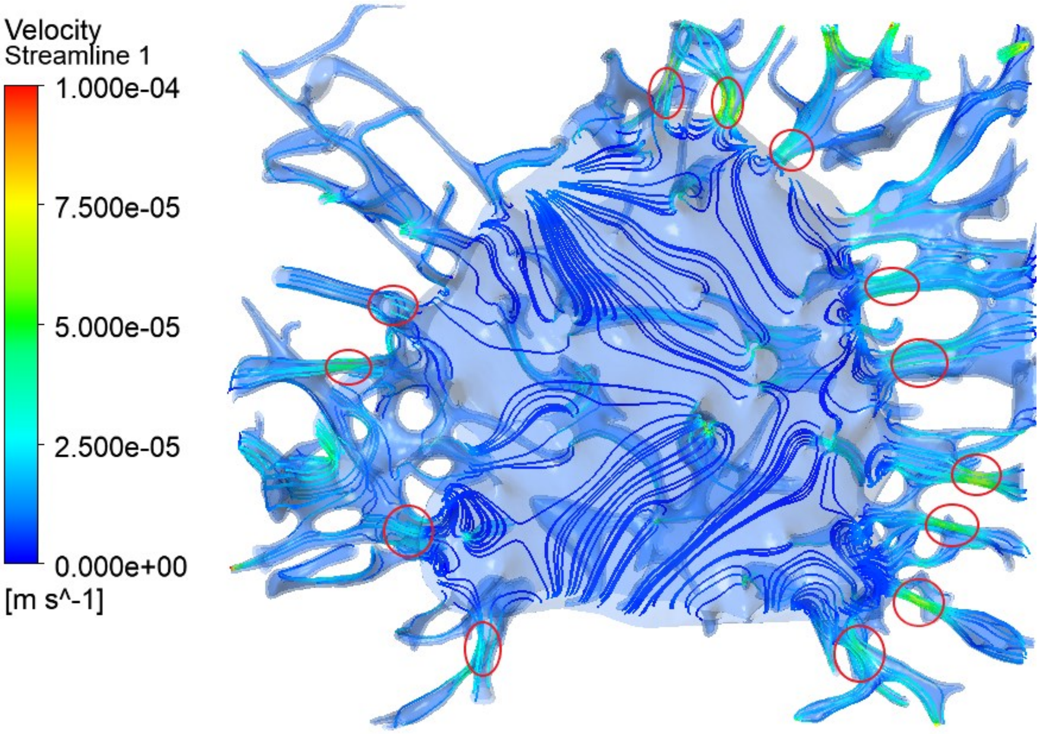

Figure 40: Cross-section of the osteocyte from the top view shows the velocity streamlines inside the pericellular space.

3.3 Simulated osteocyte models

The FFSS results of the young mouse (4-month-old) which was the base model (Model 1) was compared with other six simulated models generated using the geometry modification technique.

3.3.1 Comparison of FFSS in Model 1 (Realistic Young) and Model 3 (Simulated Aged)

The average FFSS on the dendrites in the young osteocyte model (Model 1) was 0.42 Pa, which is one order of magnitude higher than the average FFSS on the cell body (0.02 Pa) and about three times greater compared to the simulated aged osteocyte or Model 3 (0.13 Pa). The dendrites experienced an average FFSS of 0.38 Pa with simulated aging, while the cell body showed an FFSS of 0.01 Pa.

Table 3 shows the amount of surface area for the representative young vs. aged models that experience various ranges of shear magnitudes. The ratio of dendritic surface area to osteocyte is six times greater in the young osteocyte model. The young model has a larger surface area for almost all ranges of FFSS. The difference between the surface area of the two models is most significant for shear ranges above 0.1 Pa. About 76% of the surface area of the simulated aged model and 31% of the young model experiences a FFSS less than 0.1 Pa. The amount of surface area with FFSS values between 0.1 Pa and 0.8 Pa in the young osteocyte is eight times greater than the simulated aged model. It was postulated that the minimum FFSS that may cause bone formation is 0.8 Pa [9, 15]. According to data in Table 3, the amount of surface area that experiences FFSS between 0.8-3 Pa in the young model is nearly 23 times larger than the simulated aged model. Furthermore, 18% of the entire domain in the young osteocyte model, specifically dendrites, reaches 0.8 Pa, compared to only 3% in the simulated aged osteocyte model. Less than 0.2% of the surface area in both models reach FFSS higher than 3 Pa.

Table 3: Surface area of young and simulated aged models with FFSS in various ranges

		FFSS< 0.1 Pa	0.1 Pa <FFSS< 0.8 Pa	0.8 Pa <FFSS< 3 Pa	FFSS> 3 Pa
Lacunocanalicular surface area (μm^2)	Young model	1030	1630	562	7
	Simulated aged model	857	231	24	5

3.3.2 Comparison of FFSS, Surface Area, Volume of All Simulated Models

The average FFSS was 0.27 Pa and 0.13 Pa for Model 2 (simulated middle-age) and Model 3 (simulated aged), respectively. By increasing dendrite diameter to two-fold and four-fold, the average FFSS was 0.49 Pa (Model 4) and 0.57 Pa (Model 5). The osteocyte models with greater lacunocanalicular thickness of two-fold and four-fold had the highest average FFSS of 1.17 Pa (Model 6) and 1.89 Pa (Model 7). The maximum FFSS on the dendrites in the young osteocyte model was 6.6 Pa, which is two orders of magnitude higher than the FFSS on the cell body, 0.05 Pa. With simulated modeling, the maximum FFSS was 9.45 Pa, 15.46 Pa, 8.78 Pa, 6.52 Pa, 16.5 Pa, and 22.29 Pa for Model 2, Model 3, Model 4, Model 5, Model 6, and Model 7.

Table 4 shows seven distinct models including the original model and six simulated models with the details about their lacunocanalicular surface area, lacunocanalicular space volume, and average FFSS. The surface area of the lacunocanalicular space was 2652.9 μm^2, 1530.4 μm^2, 1122.6 μm^2, 3724.9 μm^2, 4791 μm^2, 3116.3 μm^2, and 3542.2 μm^2 for Model 1, Model 2, Model 3, Model 4, Model 5, Model 6, and Model 7. The simulated aged model (Model 3) had the lowest lacunocanalicular surface area and Model 5 with the largest dendrite diameter had the highest lacunocanalicular surface area. The lacunocanalicular space volume was 261 μm^3, 242.6 μm^3, 203.5 μm^3, 302.9 μm^3, 337 μm^3, 440.6 μm^3, and 658.2 μm^3 for Model 1, Model 2, Model 3, Model 4, Model 5, Model 6, and Model 7. Model 3 with lowest canalicular density had the lowest amount of lacunocanalicular space volume and Model 7 with greatest lacunocanalicular space thickness had the highest lacunocanalicular space volume.

Table 4: Comparison of average FFSS, lacunocanalicular space volume, and surface area in eight distinct osteocyte models including two confocal image-based models and six simulated models generated from Model 1 using the geometry modification technique.

Osteocyte Models	Dendrite diameter	Lacunocanalicular space thickness	Lacunocanalicular surface area (μm^2)	Lacunocanalicular volume (μm^3)	Ave FFSS (Pa)
Model 1 (original)			2652.9	261	0.42
Model 2			1530.4	242.6	0.27
Model 3			1122.6	203.5	0.13
Model 4	*2		3724.9	302.9	0.49
Model 5	*4		4791	337	0.57
Model 6		*2	3116.3	440.6	1.17
Model 7		*4	3542.2	658.2	1.89

Figure 41 shows the correlation of lacunocanalicular surface area with FFSS experienced on the cell membrane and dendritic walls for all osteocyte models. The surface area of the lacunocanalicular network increases with increasing either dendrite diameter, lacunocanalicular space thickness, and dendrite number but the FFSS does not significantly change with larger dendrite diameter. Only increasing the lacunocanalicular space thickness and dendritic number increase the FFSS. Model 5 and Model 6 with higher lacunocanalicular thickness have higher FFSS values. Although the dendrites diameter in Model 4 and Model 5 was much larger than Model 1, they do not experience a significant increase in FFSS values on cellular and dendritic walls.

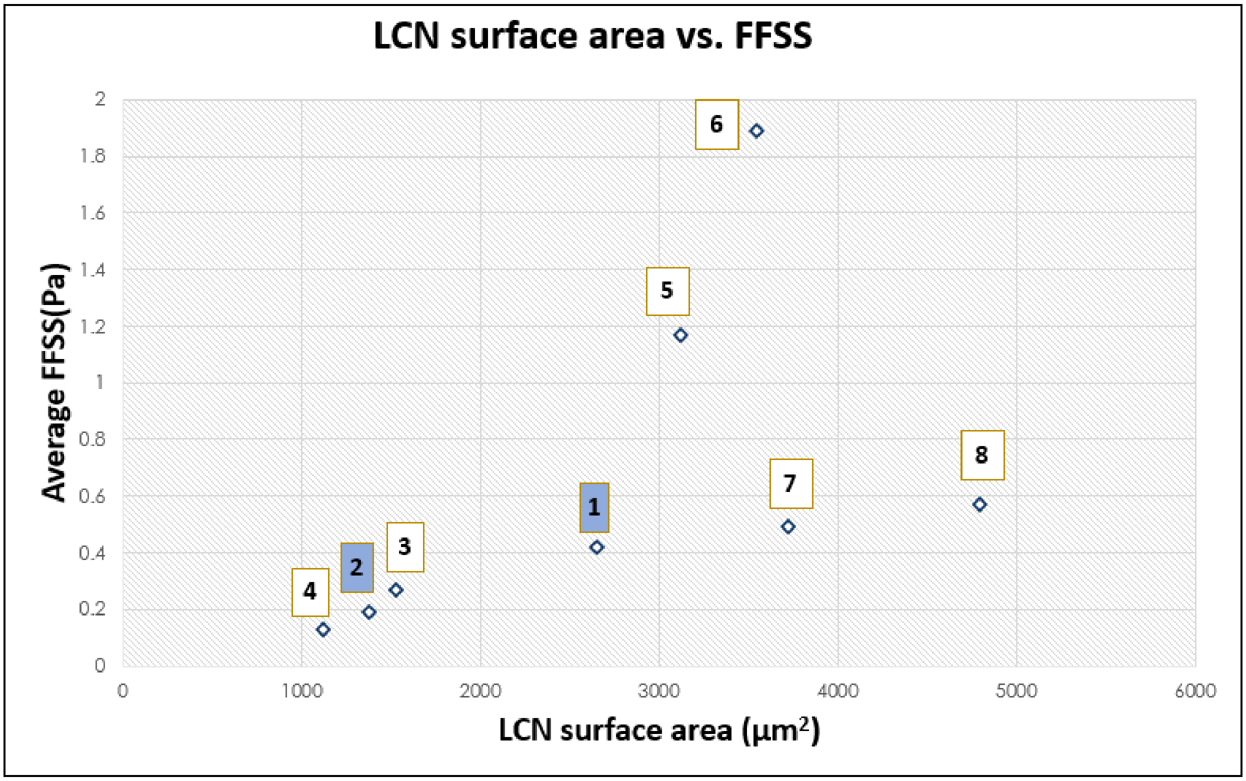

Figure 41: Comparison of lacunocanalicular surface area with FFSS for simulated models generated from Model 1. Model 2 and 3 studied lower canalicular density and lower surface area have lower FFSS. Model 4 and Model 5 with increased dendrite diameter 2-fold and 4-fold do not experience a significant increase in FFSS while they have the highest lacunocanalicular surface area. Model 6 and Model 7 with increased canalicular space thickness 2-fold and 4-fold have greatest FFSS. The correlation coefficient between Average FFSS and LCN surface area for this graph is 0.51. The green boxes show the model that produced average shear stress based on its calculated surface area.

Figure 42 shows the correlation of lacunocanalicular space volume and FFSS experienced by the osteocyte. FFSS and volume are directly proportional to each other. By increasing the lacunocanalicular space volume around the osteocyte and dendrites, FFSS increases. Increasing all the parameters including the number of dendrites, dendrite diameter, and lacunocanalicular thickness, increases the FFSS by the osteocytes. In Model 2 (middle-aged) and Model 1 (young) with two and four times greater canalicular density than Model 3 (simulated aged), fluid volume is 1.2 and 1.3 times and FFSS is about 2 and 3.2 times greater than Model 3.

In Model 4 and Model 5 with two and four times greater dendrite diameter than Model 1, the fluid volume around the cell and dendrites is 1.16 and 1.3 times greater and the FFSS experienced by the osteocyte is 1.16 and 1.35 times greater than the Model 1. Model 6 and Model 7 with two and four times greater LCN volume than Model 1, the fluid volume is about 1.7 and 2.5 times greater and the FFSS experienced by the osteocyte is about 2.8 and 4.5 times greater than Model 1.

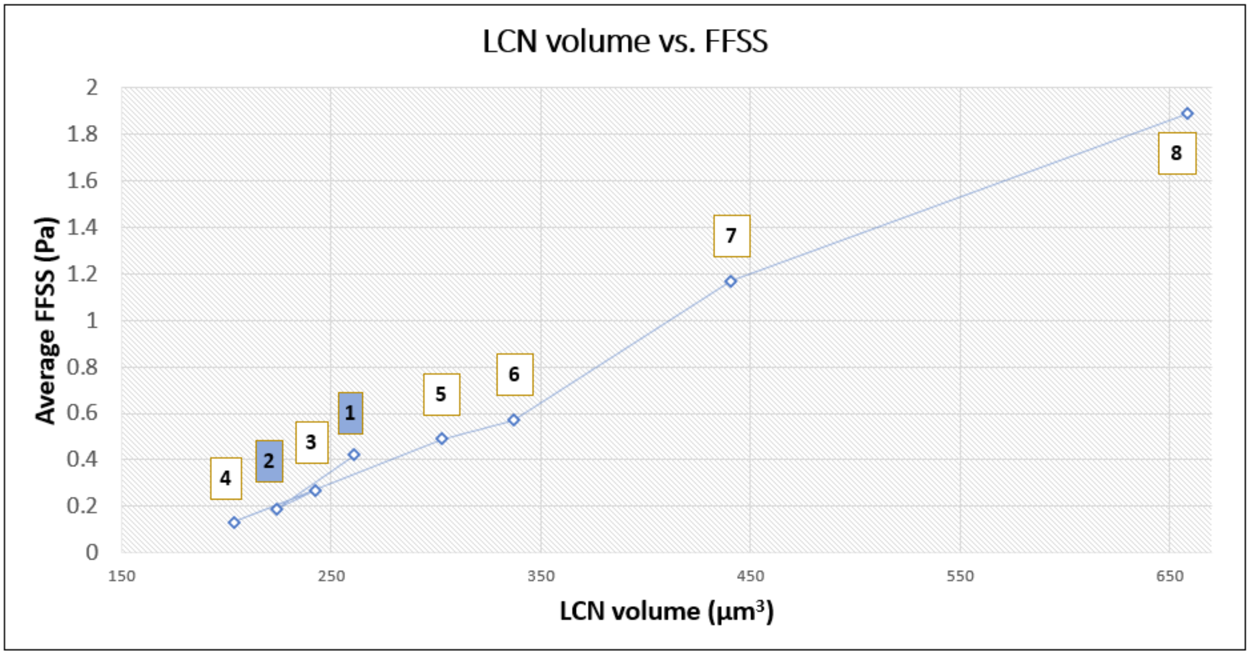

Figure 42: Comparison of lacunocanalicular space volume with FFSS in all simulated models generated from Model 1. Model 2 (simulated middle-age) and Model 3 (simulated aged) have lowest fluidic volume and FFSS. The correlation coefficient between Average FFSS and LCN fluidic space volume for this graph is 0.99 which is statistically significant. The green boxes show the model that produced average shear stress based on its calculated surface area.

3.3.3 FFSS Contours

Figure 43 depicts the FFSS contours of the original young osteocyte model (Model 1) which was obtained from the confocal FITC imaging of a 4-month-old mouse.

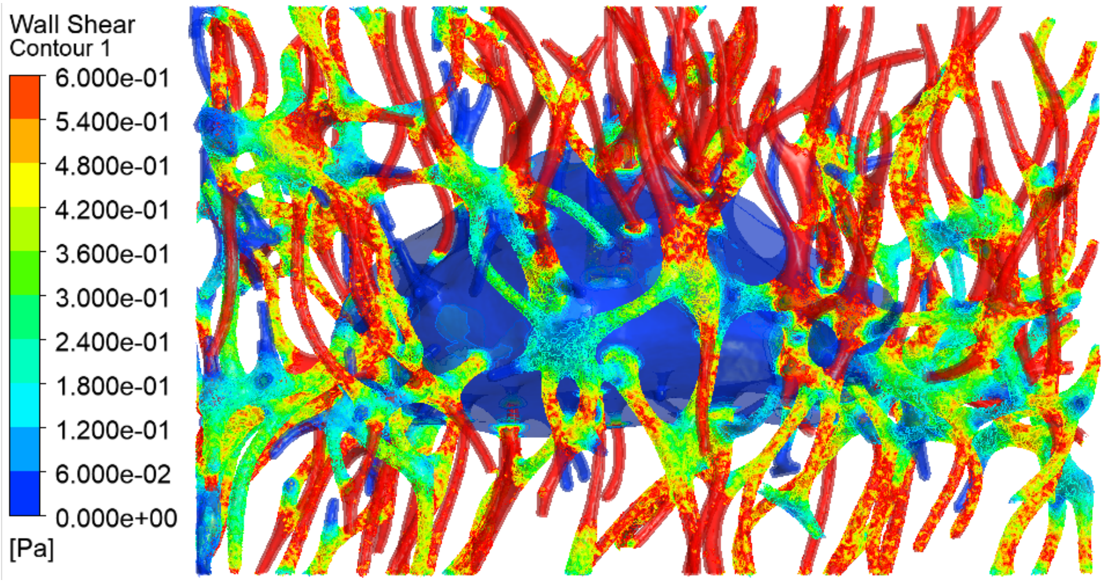

Figure 43: FFSS contours of Model 1 which was generated from FITC images of the femur of a 4-month-old mouse

Figure 44 shows the FFSS contours of the simulated middle-age osteocyte model (Model 2) with lower canalicular density compared to the realistic young osteocyte model (Model 1), but the same dendrite diameter and lacunocanalicular space thickness. Model 2 experienced a lower average FFSS (0.27 Pa) than Model 1.

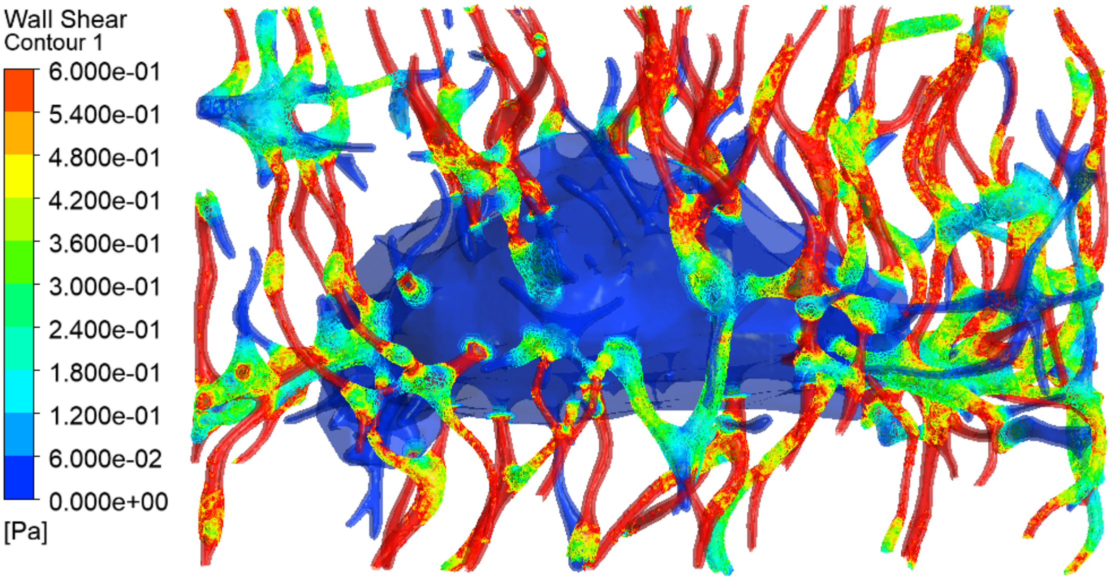

Figure 44: FFSS contours of Model 2 which has lower canalicular density than Model 1

Figure 45 depicts FFSS contours on the cell and dendritic surfaces of the aged osteocyte model (Model 3) which represents a simulated aged osteocyte with fewer dendrites compared to Model 1 and Model 2. Model 3 had the lowest lacunocanalicular surface area (1122.6 μm^2), lowest lacunocanalicular space volume (203.5 μm^3), and lowest average FFSS (0.13 Pa) among the models.

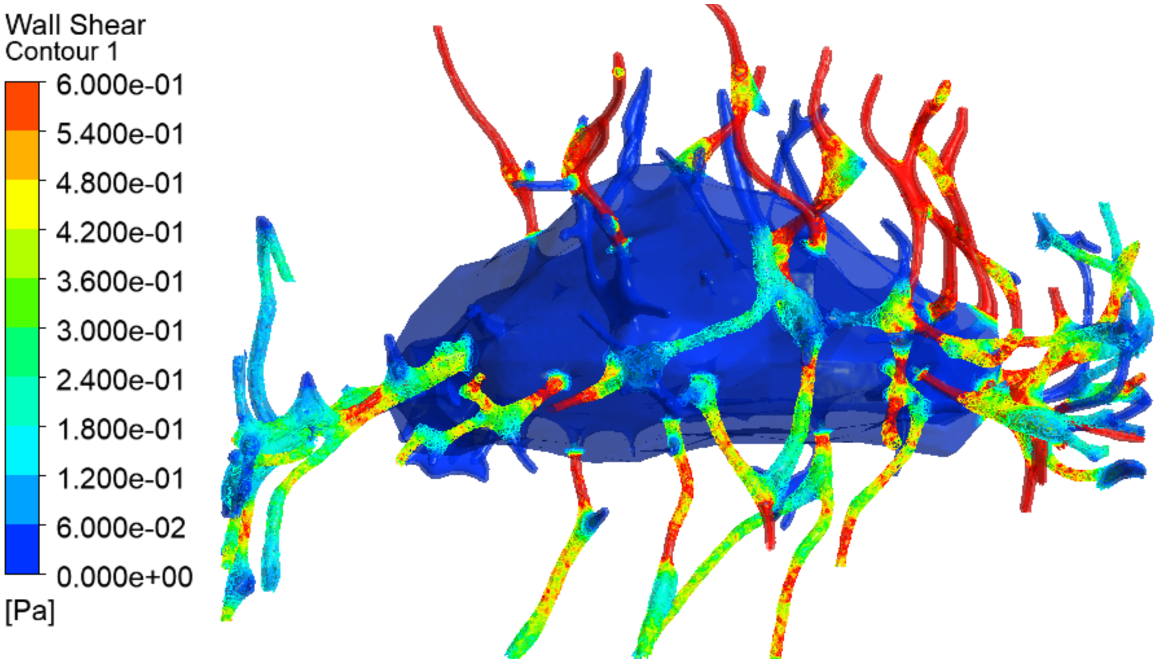

Figure 45: Contour plots of FFSS in simulated aged model (Model 3)

Figures 46 and 47 depict FFSS contours for Model 4 and Model 5 that had a two and four times greater dendrite diameter. Model 5 had the greatest lacunocanalicular surface area (4791 μm^2) among all the models and an average FFSS of 0.57 Pa.

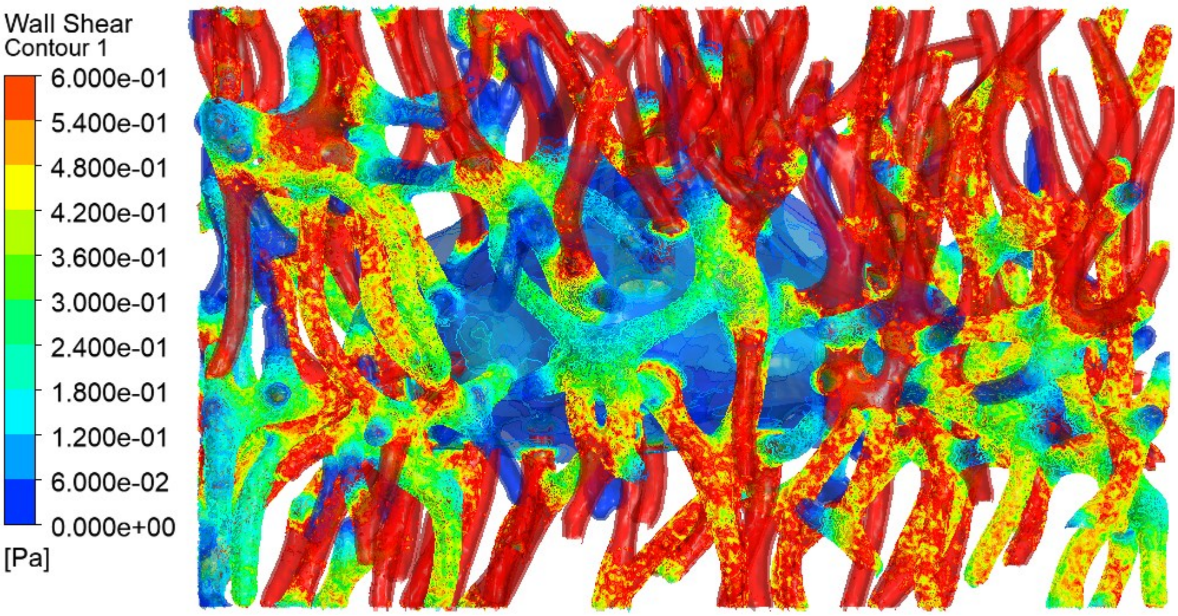

Figure 46: FFSS contours of Model 4 with two times greater dendrite diameter than Model 1

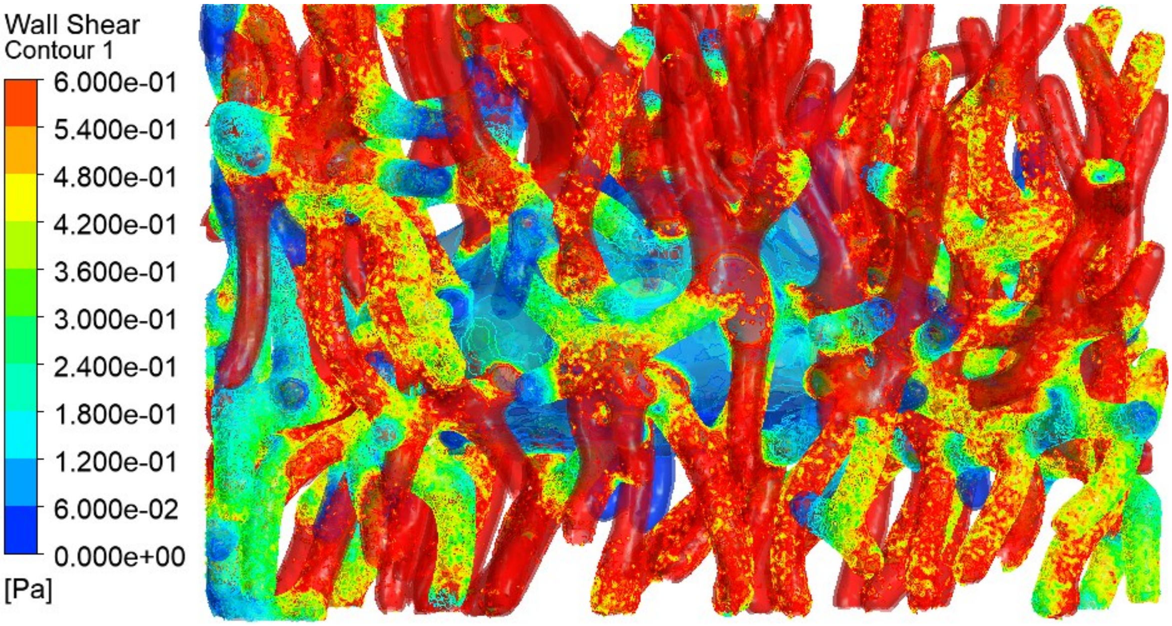

Figure 47: FFSS contours of Model 5 with four times greater dendrite diameter than Model 1

Figures 48 and 49 depict FFSS contours for Model 6 and Model 7 that had a two and four times greater lacunocanalicular space thickness. Model 7 had the greatest lacunocanalicular space volume (658.2 μm^3) among all the models. These figures show the highest amount of

FFSS among all the osteocyte models and almost all the dendritic processes are shown in the red color. Also, the cell body itself had greater shear stress values in the range of 0.2 Pa to 6.4 Pa.

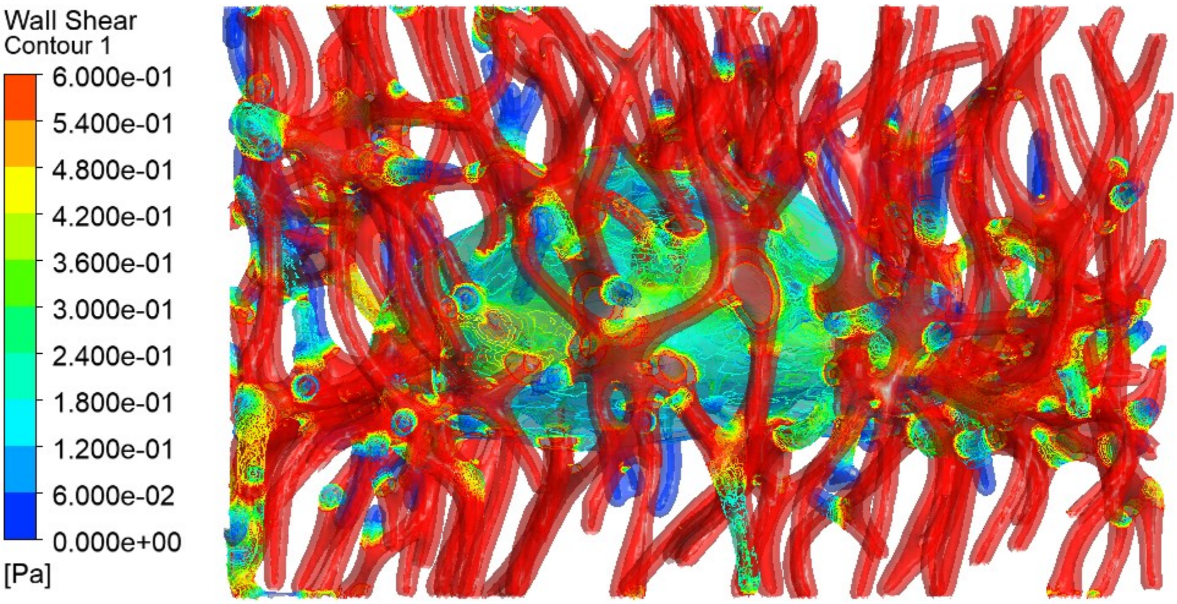

Figure 48: FFSS contours of Model 6 with two times greater lacunocanalicular space thickness than Model 1

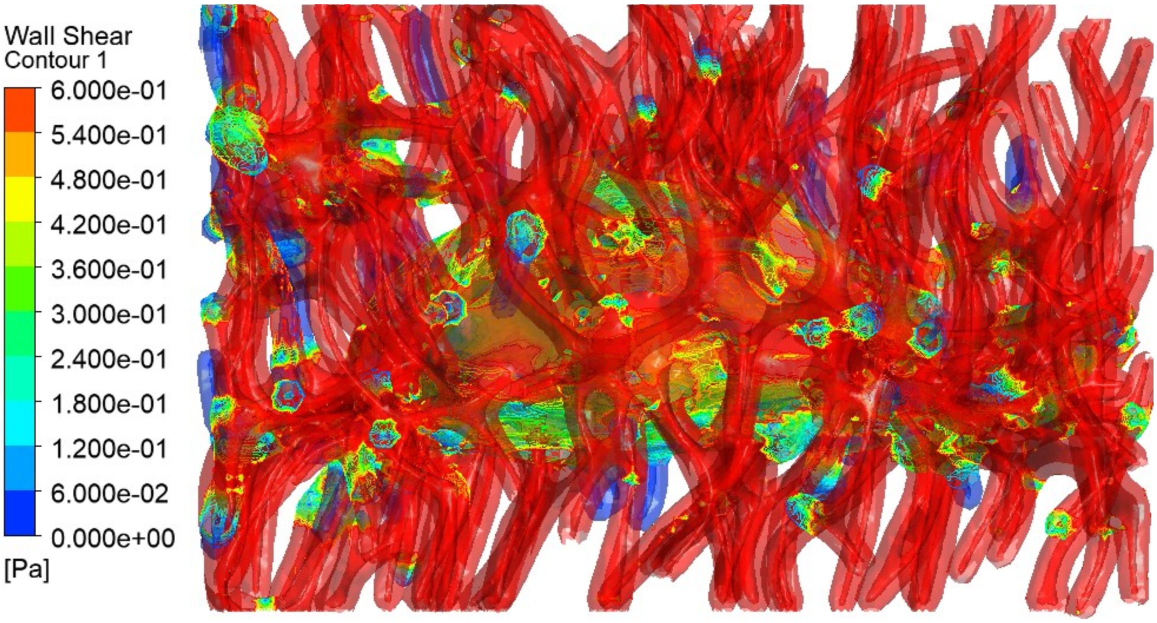

Figure 49: FFSS contours of Model 7 with four times greater lacunocanalicular space thickness than Model 1

3.3.4 Velocity

The velocity profile in all simulated models evaluated by comparing the average and maximum velocity experienced in the lacunocanalicular space. Similar to the young and aged models, simulated models have higher velocities in the canaliculi than the lacuna. In each model, the top canaliculi have higher velocities than the canaliculi on the other five sides of the osteocyte model. The average velocity in Model 1, Model 2, Model 3, Model 4, Model 5, Model 6, and Model 7 is 1.35e-5 m/s, 1.02e-5 m/s, 3.28e-6 m/s, 1.58e-5 m/s, 1.8e-5 m/s, 1.71e-5 m/s, and 2.02e-5 m/s. It is noticeable that with increasing each of the parameters of canalicular density, dendrite diameter, and lacunocanalicular thickness the average velocity increases for the simulated osteocyte models. The maximum velocity experienced by the osteocytes in Model 2 and Model 3 with lower canalicular densities are 9.84e-4 and 7.29e-4 m/s similar to the realistic young osteocyte model 7.54e-4 m/s m/s. Model 4, Model 5 with a greater dendrite diameter than Model 1 have a higher maximum velocity of 1e-3 m/s and 1.4e-3 m/s than Model 1. Model 6 and Model 7 with greater annular space than Model 1 have maximum velocity of 8.664-4 m/s and 1.1e-3 m/s.

3.3.4.1 Velocity Streamline Contours

Velocity streamline inside the lacunocanalicular space shows the fluid flow. It illustrates that fluid flows from the canaliculi selected as inlets on the upper side and goes inside the lacuna and out from the other canaliculi assigned as outlets. Figure 50, Figure 51, and Figure 52 show the velocity streamlines for Model 1 (original young osteocyte model), Model 2 (middle-aged), and Model 3 (aged), respectively. Although velocity profile of Model 1 was previously shown, we provided it again in this part to be compared with the six simulated models generated from Model 1. With reducing the number of dendrites due to aging in Model 2 and Model 3, the average velocity decreases compared to Model 1.

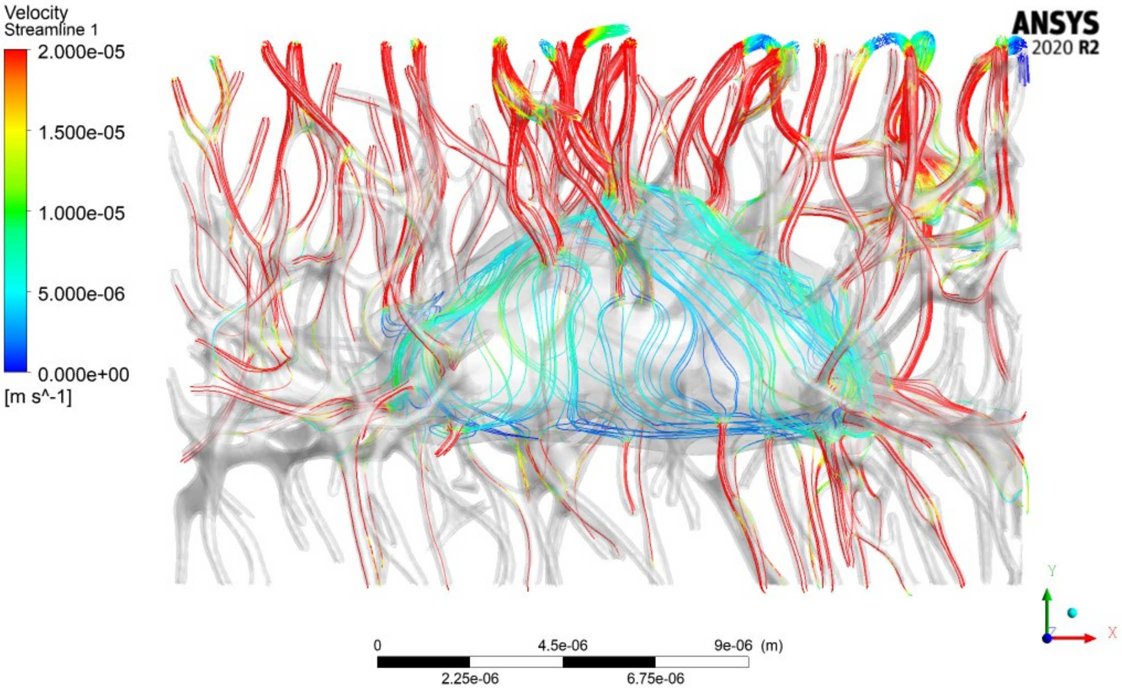

Figure 50: Velocity streamlines in realistic young osteocyte model (Model 1) generated from confocal images of a 4-month-old mouse

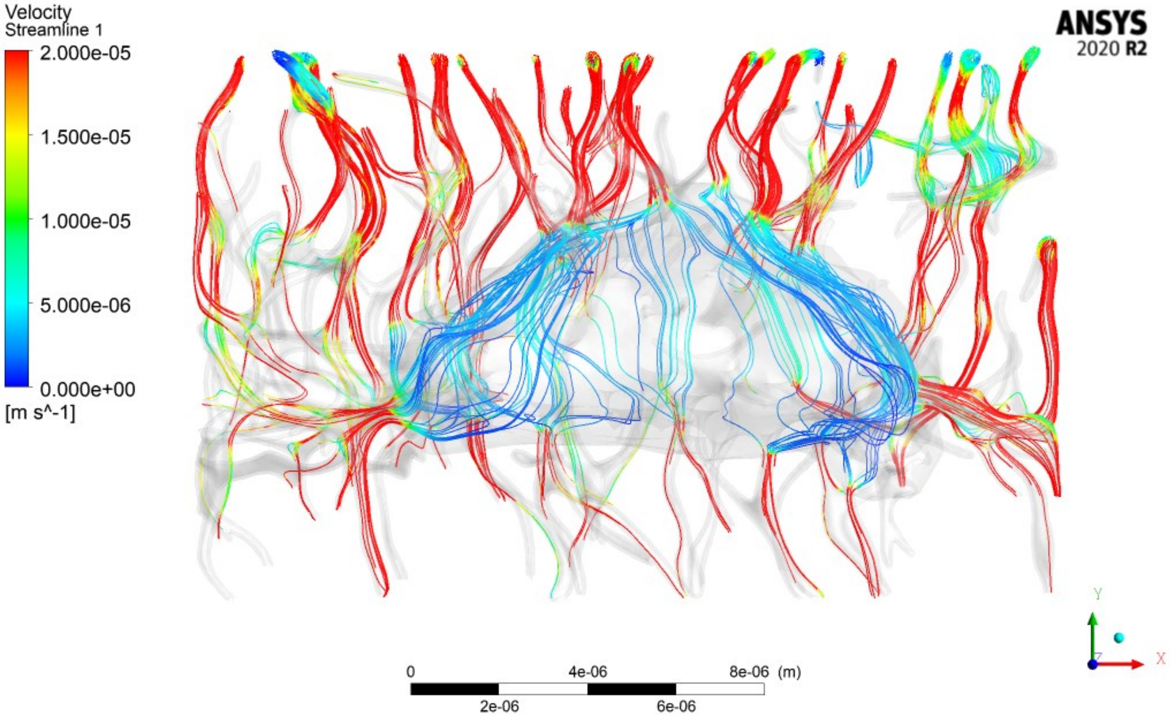

Figure 51: Velocity streamlines in simulated middle-aged osteocyte (Model 2) with lower canalicular density than realistic young osteocyte (Model 1)

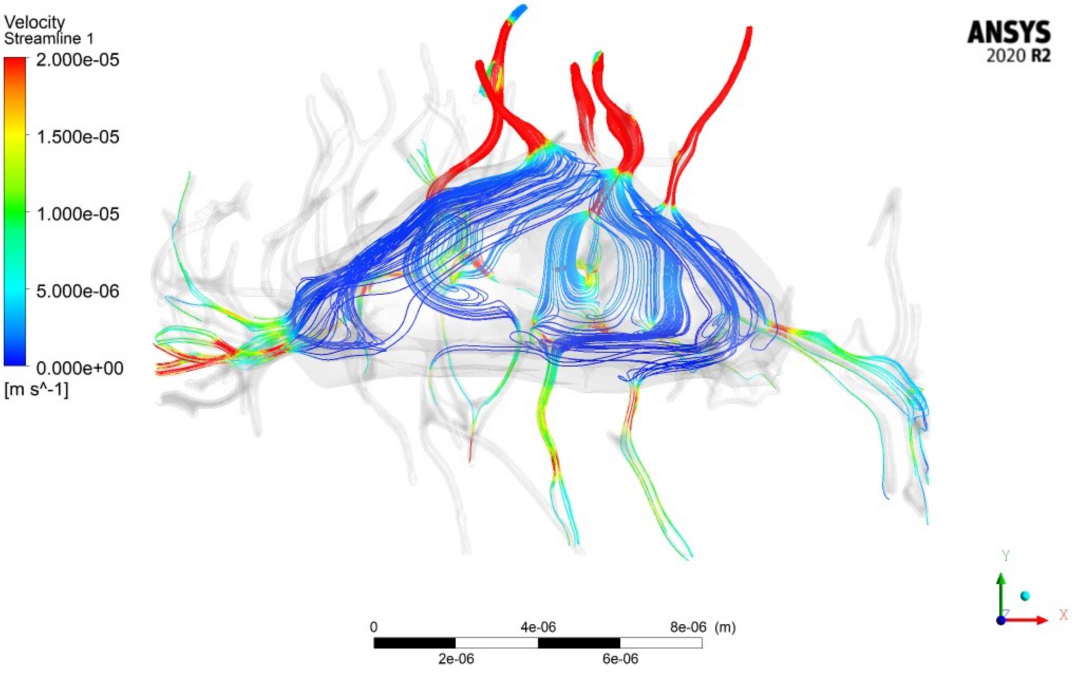

Figure 52: Velocity streamlines in Model 3 (simulated aged model)

Figure 53 and Figure 54 shows the velocity streamlines for Model 4 and Model 5. Increasing the dendrite diameter two and four times in Model 4 and Model 5, increases the maximum fluid velocity around the osteocyte and dendrites. By comparing the velocity streamlines of these two models with Model 1, it is noticeable that the velocity of fluid inside the lacuna is greater (shown in green color ~ 1e-5 m/s) by increasing the diameter of dendrites.

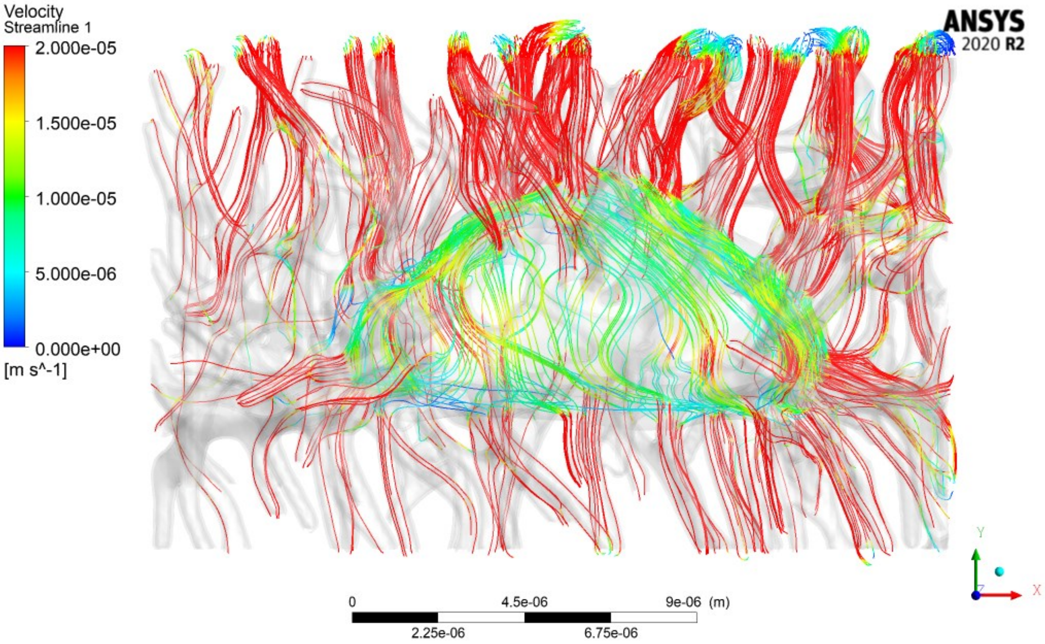

Figure 53: Velocity streamlines in Model 4 with two times greater dendritic diameter than Model 1

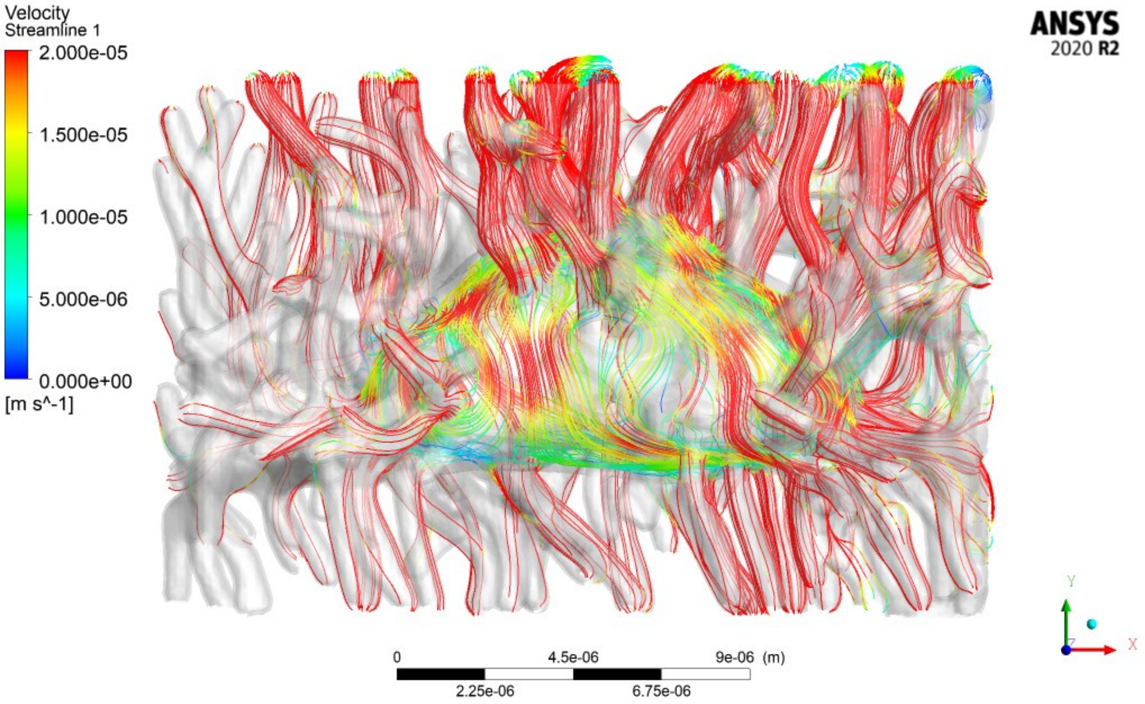

Figure 54: Velocity streamlines in Model 5 with four times greater dendritic diameter than Model 1

Figures 55 and Figure 56 shows the velocity streamlines for Model 6 and Model 7. Increasing the lacunocanalicular thickness by two and four times in Model 6 and Model 7, increases the average fluid velocity around the osteocyte and dendrites from 13.5 μm/s to 17.1 μm/s in Model 6 and 21.4 μm/s in Model 7. It is noticeable that even the cell body in these two models have higher velocities (shown in red) than the other osteocyte models. These two models have the highest velocities compared to all simulated models. It shows the effect of increasing lacunocanalicular space on the fluid velocity profile.

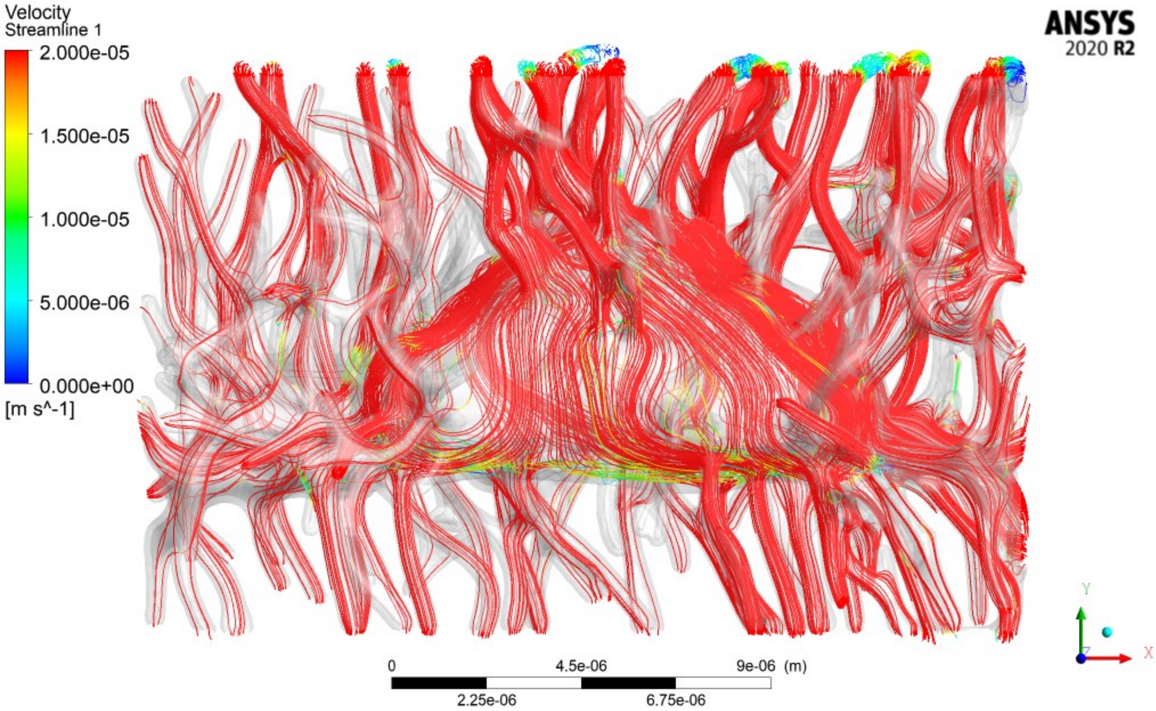

Figure 55: Velocity streamlines in Model 6 with two times greater lacunocanalicular thickness than Model 1

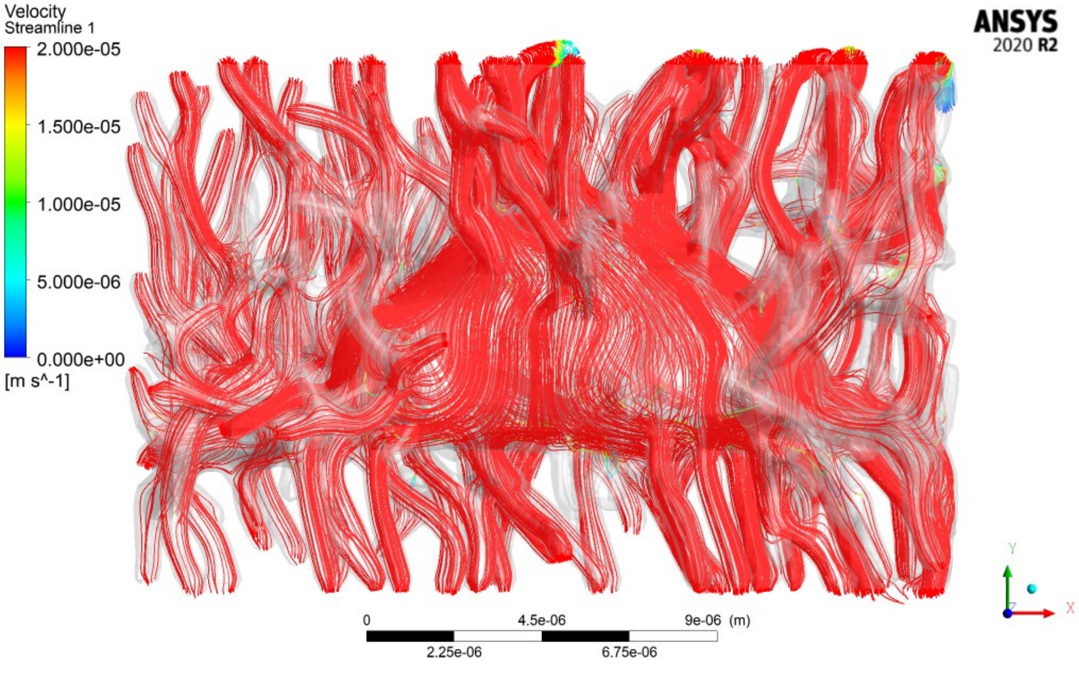

Figure 56: Velocity streamlines in Model 7 with four times greater lacunocanalicular thickness than Model 1

3.4 Comparison of Confocal Image-Based Osteocyte Model and Idealized Models

Figure 57 represents the velocity streamlines in the idealized and confocal-based models. The velocity variation within a single canaliculus is significant in the confocal-based models. Since each canaliculus in the idealized model is entirely straight, there is no sudden change in the velocity along each canaliculus (62A & 62B). Conversely, the canalicular tortuosity (shown in Figures 57C, 62D, 62E) in the image-derived realistic model speeds up the fluid in narrower regions, leading to velocity fluctuations along canaliculi. For instance, the velocity in canaliculi (Figure 57E) increases from 20.47 µm/s to 27.24 µm/s in the red-color region.

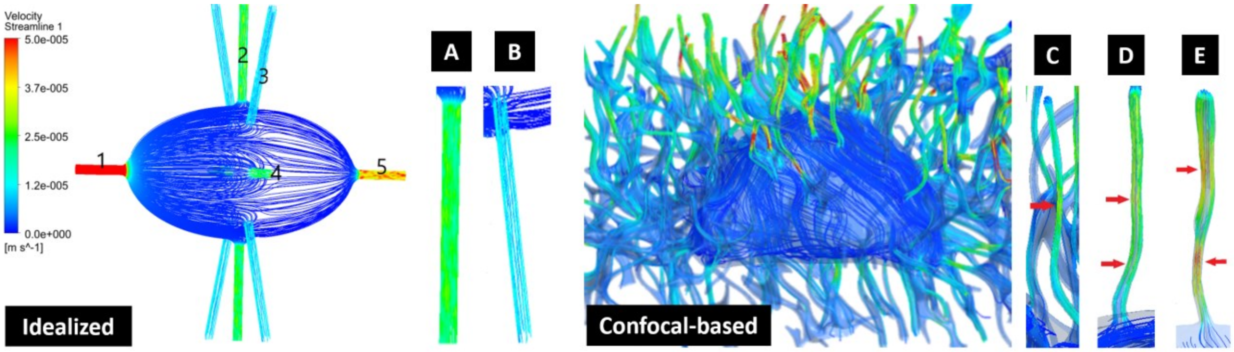

Figure 57: Idealized modeling indicates a constant velocity on single canaliculi (A), (B), while the confocal- based model shows alterations in fluid velocity profiles in (C), (D), (E)

4 CHAPTER 4: DISCUSSION

How the (micro)-architecture of the lacunocanalicular system in bone contributes to the process of mechanotransduction and how this is altered with aging is not fully understood. Interstitial fluid flow surrounding the osteocyte exerts shear stress on the cell membrane and dendritic processes beside its other functions, including delivering nutrition, eliminating waste, and facilitating cell-to-cell communication through the LCN [9, 44, 45]. One of the changes in osteocyte morphology due to aging is the reduction in canalicular density that may be a reason for the osteocyte's reduced mechano-sensitivity to mechanical loading [18-21]. We produced four models with idealized geometries of osteocytes, three image-derived realistic models, and six simulated models generated using geometry modification techniques to investigate the effect of alterations in LCN morphology due to aging on fluid flow shear stress inside the lacunar and canalicular network in response to a standardized load input.

Our idealized and young vs. aged osteocyte simulations demonstrated that dendrites have higher shear stress values, as high as 6.6 Pa, that are at least an order of magnitude higher compared to the cell body. The considerable space around the osteocyte cell body reduces the fluid velocity and FFSS in the lacuna compared to the canaliculi as well as enabling the lacuna to act as a mixing chamber [7]. Furthermore, the magnitude of shear stresses (3-6.6 Pa) in our models are in the same range as other studies which used idealized geometries for single osteocytes [23, 31]. Because of the higher shear stresses on the dendrites versus the cell body, these models suggest it is more likely that intracellular signaling in response to FFSS is triggered on the dendrites. Our findings are therefore in agreement with several functional studies suggesting that the dendrites are more responsive to load stimuli compared to the cell body [23, 42, 43].

For most previous studies, fluid shear stress measurements were primarily limited to reporting the maximum or average FFSS [23, 31]. In the current study, we estimated what proportion of the surface area of the cell and dendritic walls experiences FFSS values above 0.8 Pa, which plays a crucial role in initiating intracellular signaling associated with mechanotransduction [9, 15]. We did not compare the shear stresses of idealized and image-derived models since they have a different number of dendrites. In the idealized models, we studied two parameters, namely canalicular density and number of fluid inlets. We demonstrated that increasing canalicular density per se without changing the number of fluid inlets does not significantly affect the shear values. We postulate that contributing more canaliculi as fluid inlets drives a higher flow rate and, consequently, higher FFSS on the cell processes and the osteocyte cell body. In an osteocyte with a higher number of canaliculi and fluid inlets, mechanical loading applies additional fluid pressure to the osteocyte through the fluid inlets and consequently, more dendrites are stimulated up to the shear stress threshold of 0.8 Pa. Therefore, increasing the dendrite number may result in the osteocyte being more responsive to physical activity.

Additionally, we measured the ratio of dendritic to osteocyte surface area and also the amount of volume and surface area that experiences various ranges of FFSS, which has not been evaluated in prior studies. Comparing image-derived models showed that the ratio of dendritic to osteocyte surface area of the young model is six times greater than the aged model, while its average FFSS is three times greater than the aged model. Therefore, there might be a correlation between dendritic network surface area and fluid shear stress. With applying mechanical load to the osteocyte, due to higher canalicular density and number of fluid inlets in the young osteocyte, some additional fluid pressure is exerted in the lacunar and canalicular fluid spaces. Furthermore, we demonstrated that the surface area of the young osteocyte model with minimum shear stress for osteocyte response was 23 times greater than the aged osteocyte. Therefore, aged osteocyte with smaller dendritic regions is less possible to detect mechanical strains which explains the lower mechanoresponsiveness of osteocytes with aging with the same physiological activity. Accordingly, a larger area of the cell and dendritic surfaces in the young osteocyte model is subjected to significantly higher shear stresses, which could explain why young osteocytes respond better to mechanical loading than aged osteocytes that have lower canalicular density and fewer fluid inlets. Interestingly, the FFSS in the lacuna did not reach the bone formation threshold of 0.8 Pa in any of the confocal image-derived models and was consistently at least an order of magnitude lower than the FFSS on the dendrites. Based on these results, only the dendritic processes are predicted to be involved in activating mechanoresponsive signaling pathways in osteocytes. Our theoretical modeling is in agreement with calcium flux studies that predicted higher mechano-sensitivity of dendrites compared to the cell body [42, 43, 46, 47].

Our models also support several important implications with respect to the reduced responsiveness of aged bone versus younger adult bone. We observed that the maximum shear stresses were observed on those dendrites designated as inlets and occur at the junctions of the dendrites to the osteocyte cell body, which is consistent with prior studies [29, 48]. As more dendrites were added to the models, we observed higher strain when mechanical loading was applied in a direction parallel to the major axis of the osteocyte.

One of the benefits of image-derived models over idealized models was that the tortuosity of canalicular anatomy was incorporated into the model and its influence on velocity/shear profile could be predicted. In contrast to the idealized models in which canaliculi had a straight shape, considerable variations in velocity occurred in the tortuous canaliculi in the confocal-based models. These variations were also identified before and after branching or canalicular junctions and in narrow channels. Narrow canalicular channels with smaller cross-sections had higher velocity and FFSS. These local variations could affect whether individual dendrites or regions of dendrites respond to mechanical loading induced FFSS.

Importantly, we provided a useful approach in the confocal image-derived models to generate the osteocyte and dendrites from the confocal images of lacunocanalicular network by reducing their volume in the software. Therefore, the lacunocanalicular space can be developed from these two layers to analyze fluid profile inside the lacunocanalicular network. Using this technique, we only used one dye to label the lacunocanalicular network and this layer was reduced to have the other layer, osteocyte dendritic membranes. Therefore, we did not need to use another dye to label osteocyte dendritic membranes before imaging.

We also introduced a new technique to develop geometry-modified osteocyte models without sacrificing a new mouse, which enables us to simulate the alteration of bone microstructure due to aging and would be useful to simulate alteration of bone microstructure occurring in bone diseases such as osteoporosis, perlecan deficiency, osteogenesis imperfecta, rickets/osteomalacia, diabetes, etc. This will be a useful predictive tool for future studies to understand different bone disease states, taking into account the disease-related changes in cell morphology. It also allows us to change one feature of the model at a time (e.g., canalicular number, lacunar and canalicular size and cell body size, canalicular branching, etc.) to isolate the effects of different compartments.

Using the geometry modification technique, we used confocal images of a young mouse to mimic the morphology of aged osteocytes by modifying parameters such as canalicular density, lacunocanalicular space, dendrite diameter. One of the benefits of the geometry modification technique was that the geometry of osteocyte was kept the same and only one of the parameters of dendrite diameter, lacunocanalicular space thickness, and canalicular density was changed.

Various simulated osteocyte models were developed using the geometry modification technique to investigate whether the FFSS experienced by the osteocyte is correlated with the LCN morphology. The results showed that the FFSS significantly increases by increasing lacunocanalicular space and canalicular density. For instance, since changing the dendrite diameter does not affect the lacunocanalicular space volume and results in a wider dendrite and canaliculus, it does not significantly change the FFSS profile. On the other hand, either increasing the canalicular density or lacunocanalicular thickness increases the fluid volume applied to the cell and consequently affects the FFSS sensed by the osteocyte. Interestingly, the FFSS of the simulated models was directly proportional to the lacunocanalicular space volume with a correlation coefficient of 0.99. Therefore, the parameters that affect the lacunocanalicular space volume change the FFSS owing to their effect on fluid pattern. By only evaluating the lacunocanalicular space volume of the osteocytes, we can estimate the average FFSS experienced by the osteocyte. This is while the lacunocanalicular surface area is not such a useful tool due to the stated example about the dendrite diameter in which the surface area increases but the FFSS does not change significantly.

We compared aged osteocyte models developed using two different approaches. First, we developed it based on actual confocal images of a 22-month-old mouse. In the second approach, we developed the aged osteocyte model by reducing canalicular density of an osteocyte model from a 4-month-old mouse using the geometry modification technique. In this approach, the lacunar morphology does not change and only the effect of deterioration of the canalicular network (canalicular loss) on the FFSS was examined. The surface area and volume of the lacunocanalicular space and the range of FFSS in both methods is shown in the following table:

Table 5: Comparison of surface area and volume of the lacunocanalicular space with FFSS for young and aged osteocyte models generated using different techniques

		Lacunocanalicular surface area (μm^2)	Lacunocanalicular space volume (μm^3)	FFSS (Pa)
Confocal	Young (5-mo-old)	3102.3	333.6	0.3
	Aged (22-mo-old)	1372.7	229.4	0.19
Simulated	Young (4-mo-old)	2652.9	261	0.42
	Aged (simulated)	1122.6	203	0.13

Although the actual aged and simulated aged osteocyte models were developed from a young and an aged mouse, respectively, they showed similar FFSS results. The experienced FFSS by the osteocytes in all four models of young and aged osteocytes was proportional to surface area and volume of lacunocanalicular space. This validates the geometry modification technique as powerful predictive tool that can be applied to study the effects of aging and other diseases or conditions that affect bone mictrostructure.

One limitation of our model is that surface roughness was not considered in our analysis because we employed a smoothing technique in generating and replicating the models. As a result, some of the local projections of the extracellular matrix into the canalicular space and the surface roughness at the canalicular walls that may also affect the velocity profile [32] were not modeled in our computer simulations. Another limitation is that our model assumes that all canaliculi are occupied by a dendrite, which may not necessarily be the case, as reported by Tiede-Lewis et al[17]. Another limitation was the overstretched and oversized canalicular shapes which were captured using confocal microscopy. We reduced their size using smoothing operation in MIMICS software to achieve the correct dimensions for canaliculi and dendrites [49].

The method to generate osteocyte models using either idealized geometries or confocal image-based models and simulated models is very useful in understanding how aging effects the ability of the cells to receive signals. This provides the basis of fluid shear stress experienced by the osteocyte during physical activity and will help in establishing the connection of these stresses with the osteocyte mechano-sensation due to aging. Eventually, it can help in developing therapies that can maintain the quality of bone in different bone diseases by checking the LCN morphology and especially the volume of lacunocanalicular space. This study gives a detailed methodology that describes the computational modeling of osteocytes and characterize osteocyte morphology. In addition, it reveals the influence of geometrical parameters on osteocyte fluid flow shear stress. This data gives the insight of how osteocyte behave with morphological changes due to aging.

Overall, the shear stress stimulation decreases with decreased canalicular density due to aging. The loss of osteocyte dendritic connectivity in aged mice could therefore explain reduced responsiveness to mechanical loading in older animals.

5 CHAPTER 5: CONCLUSION AND FUTURE WORK

The objective of this research was to determine if there is a correlation between LCN deterioration due to aging in terms of reduction in canalicular density or surface area and the resulting changes in shear stresses that would be experienced by osteocytes and their dendrites. The current study explored various approaches for generating computer models of osteocytes that incorporate features of the lacunocanalicular system due to aging. Idealized Fluid-Structure Interaction models, confocal image-based models, and simulated models using geometry modification techniques were used to determine the lacunar fluid shear stresses on the membrane of the cells and dendrites at the single-cell level.

We determined the effect of changing the canalicular density, fluid inlets to the lacuna, and the orientation of the cell to the applied physiological pressure. The number of canaliculi and fluid inlets played an important role in the velocity profile and in determining whether the shear stress threshold was reached that would initiate the cellular mechanostranstuction response. Because our modeling demonstrated that lower osteocyte shear stresses were associated with reduced canalicular density due to aging, measuring canalicular density could be a helpful approach in predicting osteocyte behavior in future studies. Furthermore, our findings suggest that it is possible to model aging-associated changes in osteocyte morphology and that bone mechanical stimuli may be altered by reduced lacunar and canalicular fluid flow when osteocyte connectivity is reduced due to aging. The FFSS experienced by the osteocyte can be evaluated by measuring the lacunocanalicular space volume. Our simulated osteocyte models showed that if the osteocyte morphology is kept the same, FFSS is dependent to the volume of the lacunocanalicular space. Computer modeling of the osteocyte could assess the role of LCN morphology and notably canalicular density in terms of the impaired osteocyte’s response to mechanical loading due to aging.

6 REFERENCES

1. Rachner, T.D., S. Khosla, and L.C. Hofbauer, Osteoporosis: Now and the future. The Lancet, 2011. 377(9773): p. 1276-1287.
2. Noh, J.Y., Y. Yang, and H. Jung, Molecular mechanisms and emerging therapeutics for osteoporosis. International Journal of Molecular Sciences, 2020. 21(20).
3. Parfitt, A.M., et al., Relationships between surface, volume, and thickness of iliac trabecular bone in aging and in osteoporosis. Implications for the microanatomic and cellular mechanisms of bone loss. The Journal of Clinical Investigation, 1983. 72(4): p. 1396-1409.
4. Khosla, S., Pathogenesis of age-related bone loss in humans. The Journals of Gerontology: Series A, 2013. 68(10): p. 1226-1235.
5. Riggs, B.L., S. Khosla, and L.J. Melton, 3rd, A unitary model for involutional osteoporosis: estrogen deficiency causes both type I and type II osteoporosis in postmenopausal women and contributes to bone loss in aging men. Journal of Bone and Mineral Research, 1998. 13(5): p. 763-73.
6. Li, M.C.M., et al., The role of osteocytes-specific molecular mechanism in regulation of mechanotransduction - A systematic review. Journal of Orthopedic Translation, 2021. 29: p. 1-9.
7. Fritton, S.P. and S. Weinbaum, Fluid and solute transport in bone: flow-induced mechanotransduction. Annual Review of Fluid Mechanics, 2009. 41: p. 347-374.
8. Klein-Nulend, J., R.G. Bacabac, and A.D. Bakker, Mechanical loading and how it affects bone cells: the role of the osteocyte cytoskeleton in maintaining our skeleton. European Cells and Materials, 2012. 24: p. 278-91.
9. Weinbaum, S., S.C. Cowin, and Y. Zeng, A model for the excitation of osteocytes by mechanical loading-induced bone fluid shear stresses. Journal of Biomechanics, 1994. 27(3): p. 339-360.
10. Knothe, M.T., " Whither flows the fluid in bone?" An osteocyte's perspective. Journal of Biomechanics, 2003. 36(10): p. 1409-1424.
11. Han, Y., et al., Mechanotransduction and strain amplification in osteocyte cell processes. Proceedings of the National Academy of Sciences of the United States of America, 2004. 101(47): p. 16689-16694.
12. Burger, E., Influence of mechanical factors on bone formation, resorption and growth in vitro. Bone, 1993. 7: p. 37-56.
13. You, J., et al., Substrate deformation levels associated with routine physical activity are less stimulatory to bone cells relative to loading-induced oscillatory fluid flow. The Journal of Biomechanical Engineering., 2000. 122(4): p. 387-393.
14. Carter, D.R., D.P. Fyhrie, and R.T. Whalen, Trabecular bone density and loading history: Regulation of connective tissue biology by mechanical energy. Journal of Biomechanics, 1987. 20(8): p. 785-794.
15. You, L., et al., A model for strain amplification in the actin cytoskeleton of osteocytes due to fluid drag on pericellular matrix. Journal of Biomechanics, 2001. 34(11): p. 1375-1386.
16. Nicolella, D.P., et al., Osteocyte lacunae tissue strain in cortical bone. Journal of Biomechanics, 2006. 39(9): p. 1735-1743.
17. Tiede-Lewis, L.M., et al., Degeneration of the osteocyte network in the C57BL/6 mouse model of aging. Aging, 2017. 9(10): p. 2190-2208.

18. Schurman, C.A., S.W. Verbruggen, and T. Alliston, Disrupted osteocyte connectivity and pericellular fluid flow in bone with aging and defective TGF-β signaling. Proceedings of the National Academy of Sciences, 2021. 118(25).
19. Kobayashi, K., et al., Mitochondrial superoxide in osteocytes perturbs canalicular networks in the setting of age-related osteoporosis. Scientific Reports, 2015. 5(1): p. 9148.
20. Vashishth, D., et al., Decline in osteocyte lacunar density in human cortical bone is associated with accumulation of microcracks with age. Bone, 2000. 26(4): p. 375-80.
21. Tiede-Lewis, L.M. and S.L. Dallas, Changes in the osteocyte lacunocanalicular network with aging. Bone, 2019. 122: p. 101-113.
22. Anderson, E., et al., Nano? Microscale models of periosteocytic flow show differences in stresses imparted to cell body and processes. Annals of Biomedical Engineering, 2005. 33: p. 52-62.
23. Verbruggen, S.W., T.J. Vaughan, and L.M. McNamara, Fluid flow in the osteocyte mechanical environment: a fluid–structure interaction approach. Biomechanics and Modeling in Mechanobiology, 2014. 13(1): p. 85-97.
24. Verbruggen, S.W., T.J. Vaughan, and L.M. McNamara, Strain amplification in bone mechanobiology: a computational investigation of the in vivo mechanics of osteocytes. Journal of the Royal Society, Interface, 2012. 9(75): p. 2735-2744.
25. Anderson, E.J. and M.L. Knothe Tate, Idealization of pericellular fluid space geometry and dimension results in a profound underprediction of nano-microscale stresses imparted by fluid drag on osteocytes. Journal of Biomechanics, 2008. 41(8): p. 1736-1746.
26. Haridy, Y., et al., Bone metabolism and evolutionary origin of osteocytes: Novel application of FIB-SEM tomography. Science Advances, 2021. 7(14): p. eabb9113.
27. Sharma, D., et al., Alterations in the osteocyte lacunar-canalicular microenvironment due to estrogen deficiency. Bone, 2012. 51(3): p. 488-497.
28. Kola, S.K., et al., Osteocyte lacunar strain determination using multiscale finite element analysis. Bone Reports, 2020. 12: p. 100277-100277.
29. Rath Bonivtch, A., L.F. Bonewald, and D.P. Nicolella, Tissue strain amplification at the osteocyte lacuna: A microstructural finite element analysis. Journal of Biomechanics, 2007. 40(10): p. 2199-2206.
30. Bonewald, L.F. and M.L. Johnson, Osteocytes, mechanosensing and Wnt signaling. Bone, 2008. 42(4): p. 606-15.
31. Joukar, A., H. Niroomand-Oscuii, and F. Ghalichi, Numerical simulation of osteocyte cell in response to directional mechanical loadings and mechanotransduction analysis: Considering lacunar–canalicular interstitial fluid flow. Computer Methods and Programs in Biomedicine, 2016. 133: p. 133-141.
32. Kamioka, H., et al., Microscale fluid flow analysis in a human osteocyte canaliculus using a realistic high-resolution image-based three-dimensional model. Integrative Biology, 2012. 4(10): p. 1198-1206.
33. van Tol, A.F., et al., Network architecture strongly influences the fluid flow pattern through the lacunocanalicular network in human osteons. Biomechanics and Modeling in Mechanobiology, 2020. 19(3): p. 823-840.
34. Webster, D.J., et al., Studying osteocytes within their environment. Bone, 2013. 54(2): p. 285-295.
35. You, L.D., et al., Ultrastructure of the osteocyte process and its pericellular matrix. Anatomical Record, 2004. 278(2): p. 505-13.

36. McNamara, L.M., et al., Attachment of osteocyte cell processes to the bone matrix. Anatomical record (Hoboken, N.J.: 2007), 2009. 292(3): p. 355-363.
37. Wang, L., et al., In situ measurement of solute transport in the bone lacunar-canalicular system. Proceedings of the National Academy of Sciences of the United States of America, 2005. 102(33): p. 11911-11916.
38. Burr, D.B., et al., In vivo measurement of human tibial strains during vigorous activity. Bone, 1996. 18(5): p. 405-410.
39. Schneider, P., et al., Serial FIB/SEM imaging for quantitative 3D assessment of the osteocyte lacuno-canalicular network. Bone, 2011. 49(2): p. 304-311.
40. Manfredini, P., et al., Poroelastic finite element analysis of a bone specimen under cyclic loading. Journal of Biomechanics, 1999. 32(2): p. 135-44.
41. Steck, R., P. Niederer, and M.L. Knothe Tate, A Finite Element Analysis for the Prediction of Load-induced Fluid Flow and Mechanochemical Transduction in Bone. Journal of Theoretical Biology, 2003. 220(2): p. 249-259.
42. Burra, S., et al., Dendritic processes of osteocytes are mechanotransducers that induce the opening of hemichannels. Proceedings of the National Academy of Sciences, 2010. 107(31): p. 13648-13653.
43. Lu, X.L., et al., Osteocytic network is more responsive in calcium signaling than osteoblastic network under fluid flow. Journal of bone and mineral research: the official journal of the American Society for Bone and Mineral Research, 2012. 27(3): p. 563-574.
44. Cowin, S.C., Mechanosensation and fluid transport in living bone. Journal of Musculoskeletal and Neuronal Interactions, 2002. 2(3): p. 256-60.
45. Verbruggen, S.W., T.J. Vaughan, and L.M. McNamara, Mechanisms of osteocyte stimulation in osteoporosis. Journal of Mechanical Behavior of Biomedical Materials, 2016. 62: p. 158-168.
46. Jing, D., et al., In situ intracellular calcium oscillations in osteocytes in intact mouse long bones under dynamic mechanical loading. FASEB journal: official publication of the Federation of American Societies for Experimental Biology, 2014. 28(4): p. 1582-1592.
47. Adachi, T., et al., Calcium response in single osteocytes to locally applied mechanical stimulus: Differences in cell process and cell body. Journal of Biomechanics, 2009. 42(12): p. 1989-1995.
48. Varga, P., et al., Synchrotron X-ray phase nano-tomography-based analysis of the lacunar-canalicular network morphology and its relation to the strains experienced by osteocytes in situ as predicted by case-specific finite element analysis. Biomechanics and Modeling in Mechanobiology, 2015. 14(2): p. 267-82.
49. Nango, N., et al., Osteocyte-directed bone demineralization along canaliculi. Bone, 2016. 84: p. 279-288.

VITA

Mohammad Niroobakhsh was born on July 18, 1990, in Ahvaz, Iran. He received his bachelor's degree in Mechanical Engineering from Semnan University in 2013. He received his master's degree in Automotive Engineering from Iran University of Science and Technology in 2016.

Mohammad perused his Interdisciplinary PhD degree at the University of Missouri-Kansas City. His primary PhD discipline is Engineering, and his co-discipline is Oral and Craniofacial Sciences. His research interests are in the area of bone biomechanics using the experimental techniques and computational models.